ACS OMEGA

Open Access

http://pubs.acs.org/journal/acsodf

Article

Mathematical Modeling and Optimization of Highly Efficient Nontoxic All-Inorganic $CsSnGeI_3$-Based Perovskite Solar Cells with Oxide and Kesterite Charge Transport Layers

Muhammad Noman,* Ihsan Nawaz Khan, Affaq Qamar,* Khalid AlSnaie, and Hassan M. Hussein Farh

Cite This: *ACS Omega* 2024, 9, 11398−11417

Read Online

ACCESS | Metrics & More | Article Recommendations

ABSTRACT: Despite exceptional optoelectronic properties and rapidly increasing efficiency of perovskite solar cells (PSCs), the issues of toxicity and device instability have hampered the commercialization of this renewable energy technology. Lead (Pb) being the main culprit creates major environmental risks and therefore must be replaced with a nontoxic material such as tin (Sn), germanium (Ge), etc. Moreover, replacing organic cations in the perovskite's ABX_3 structure with inorganic ones like cesium (Cs) helps aid the stability issues. This study uses six different kesterite-based hole transport layers (HTLs) and three different metal oxide-based electron transport layers (ETLs) to numerically simulate and optimize all-inorganic $CsSnGeI_3$ PSCs. Metal oxide ETLs are used in this study due to their large band gap, while kesterite HTLs are used due to their excellent conductive properties. All of the simulations are performed under standard testing conditions. A total of 18 novel planar (n-i-p) PSCs are modeled by the combination of various charge transport layers (CTLs), and the device optimization was done to enhance the power conversion efficiencies (PCEs) of the PSCs. Furthermore, the effect of CTLs on the energy band alignment, electric field, quantum efficiency, light absorption, and recombination rate is analyzed. Additionally, a detailed analysis of the impact of defect density (N_t), interface defects (ETL/Perv, Perv/HTL), temperature, and work function on the functionality of 18 different $CsSnGeI_3$-based PSCs is conducted. The simulation findings demonstrate that $SnO_2/CsSnGeI_3$/CNTS is the most efficient optimized PSC among all of the simulated structures, with a PCE of 27.33%, J_{sc} of 28.04 mA/cm^2, FF of 85%, and V_{oc} of 1.14 V.

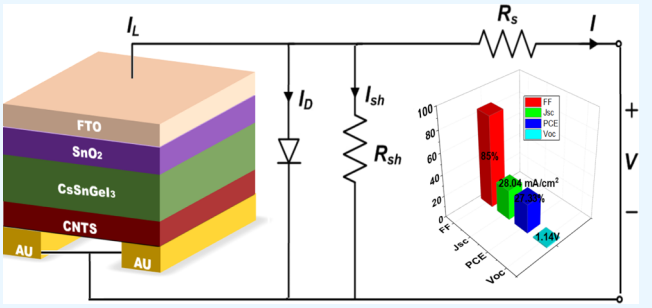

1. INTRODUCTION

Perovskites, discovered by the German scientist Gustavo Rose in 1839, are hybrid (organic−inorganic) materials possessing the ABX_3 crystal structure depicted in Figure 1[1]. In the crystal formula, "A" denotes a hybrid cation, "B" is a metal cation, and "X" is a halide anion.[2] These materials showcase remarkable optoelectronic characteristics, including efficient light absorption, adjustable band gap, extensive carrier diffusion, and versatile carrier transport. As per NREL data, lead-perovskite solar cells (Pb-PSCs) have achieved an impressive 26.1% power conversion efficiency.[3] Up to this point, the extensively studied PSCs include $MAPbI_3$ and $FAPbI_3$.

Conversely, the two extensively investigated lead-based PSCs face significant challenges related to both toxicity and instability, which have hampered the commercialization of this technology so far.[4] As Pb is easily soluble in water and has hazardous environmental impacts, researchers are looking to solve the issue by replacing Pb with some nontoxic materials such as Sn, Ge, etc.[5] Although nontoxic PSCs are less efficient as compared to Pb-PSCs, there is still a lot of room for performance improvement. Moreover, the substitution of organic cations with inorganic ones in the perovskite crystal structure helps in resolving stability issues as well.[6] Thus, inorganic PSCs are viable candidates in PV technology as they address the issues of both toxicity and thermal stability under ambient conditions.

To address toxicity concerns, researchers have extensively explored halide PSCs based on tin such as $MASnI_3$ and $FASnI_3$.[7] However, they found intrinsically low stability with these structures. To further extend the research, scientists have utilized inorganic cations such as cesium (Cs) in place of organic methylammonium (MA) and formamidinium (FA) to make all-inorganic Pb-free PSCs.[8] The literature showed that $CsSnI_3$-based PSCs can be potential candidates and a viable option for future commercialization as they have the highest power conversion efficiencies (PCEs) of any lead-free PSC.[9] However,

Received: October 6, 2023
Revised: January 26, 2024
Accepted: February 6, 2024
Published: February 27, 2024

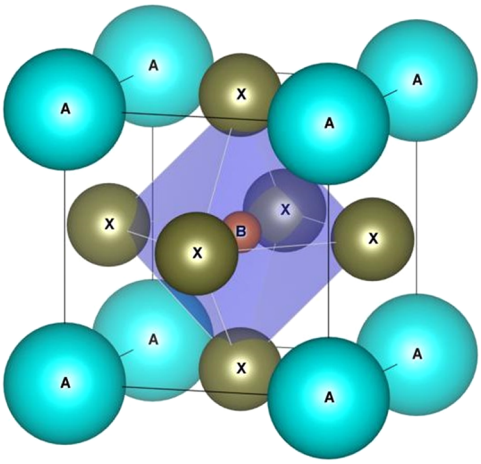

Figure 1. Crystal structure of perovskite (ABX_3).

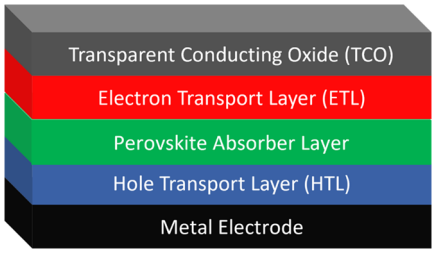

Figure 2. Architecture of the perovskite solar cell.

on the other hand, Sn(II) is rapidly oxidized to Sn(IV), and phase instability occurs in the $CsSnI_3$ perovskite, leading to the degradation of the layer properties.[10]

Chen and colleagues proposed that adding Ge to $CsSnI_3$ not only improves the stability but also enhances the output power. They found that the PCE of $CsSnGeI_3$ PSC surpasses both the $CsSnI_3$- and $CsGeI_3$-based PSCs.[11] Although Ge-based halide PSCs have shown tremendous potential in PV technology, just like Sn-based PSCs, Ge-PSCs also have issues of oxidation from Ge^{2+} to Ge^{4+}, which ultimately leads to performance degradation of the solar cell.[12] Ge-PSCs are more stable than Sn-PSCs because they have negative formation energy.[13] Various studies have also suggested the use of mixed tin−germanium to address the stability and performance issue. The mixed tin−germanium PSCs are less efficient than Pb-PSCs, but they have the potential to revolutionize the PV industry once all of the issues are overcome.[14,15]

The PSC architecture consists of five main layers positioned upon one another based on the cell's structure (planar/inverted).[16] The performance of the PSC depends directly on the device architecture and the charge transport layer (CTL) materials. To provide the proper energy band alignment and enable the flow of charge carriers from the absorber material to the appropriate electrodes, suitable CTLs must be chosen with the perovskite layer.[17] Because of the inappropriate band alignment between the various PSC layers, the combination of incompatible CTLs with perovskite material directly reduces the PV performance of the cell. Therefore, it is recommended to choose conductive CTLs that are compatible with the absorber in order to create an ideal band alignment that will make it easier for charge carriers to flow from the perovskite to the electrodes. The function of CTLs is to separate charge carriers from the absorber because of their band alignment and then transport them to the anode and cathode. To enhance the PCE of the cell, the CTLs should be conductive and less resistive in nature to provide adequate separation of charge carriers.[18,19]

In this work, a $CsSnGeI_3$ perovskite solar cell is numerically modeled and optimized with three metal oxide electron transport layers (ETLs) and with six kesterite hole transport layers (HTLs). The ETLs selected in this study are due to their

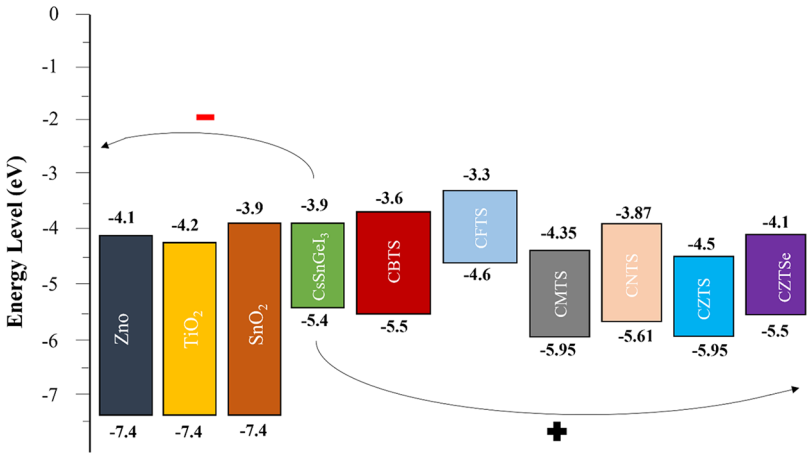

Figure 3. Energy band alignment of PSCs.

Table 1. Simulated Perovskite Solar Cell Structures

group A	group B	group C
$TiO_2/CsSnGeI_3/CBTS$	$SnO_2/CsSnGeI_3/CBTS$	$ZnO/CsSnGeI_3/CBTS$
$TiO_2/CsSnGeI_3/CFTS$	$SnO_2/CsSnGeI_3/CFTS$	$ZnO/CsSnGeI_3/CFTS$
$TiO_2/CsSnGeI_3/CMTS$	$SnO_2/CsSnGeI_3/CMTS$	$ZnO/CsSnGeI_3/CMTS$
$TiO_2/CsSnGeI_3/CNTS$	$SnO_2/CsSnGeI_3/CNTS$	$ZnO/CsSnGeI_3/CNTS$
$TiO_2/CsSnGeI_3/CZTS$	$SnO_2/CsSnGeI_3/CZTS$	$ZnO/CsSnGeI_3$ /CZTS
$TiO_2/CsSnGeI_3/CZTSe$	$SnO_2/CsSnGeI_3/CZTSe$	$ZnO/CsSnGeI_3/CZTSe$

https://doi.org/10.1021/acsomega.3c07754
ACS Omega 2024, 9, 11398−11417

Table 2. Simulated PSC Structure Parameters Used in SCAPS-1D

parameters	TiO_2	SnO_2	ZnO	$CsSnGeI_3$	CBTS	CFTS	CMTS	CNTS	CZTS	CZTSe
refs	12	24	25	14,15	26	13	27	28	13	27
thickness (nm)	150	150	150	400	150	150	150	150	150	150
band gap (eV)	3.2	3.5	3.3	1.5	1.9	1.3	1.5	1.74	1.45	1.0
electron affinity (eV)	4	4	4.1	3.90	3.6	3.3	4.35	3.87	4.5	4.2
dielectric permittivity	10	9	9	28	5.4	9	9	9	9	9.1
CB effective density of state (cm^{-3})	2×10^{18}	2.2×10^{17}	4×10^{18}	3.1×10^{18}	2.2×10^{18}	2.2×10^{18}	2.2×10^{18}	2.2×10^{18}	2.2×10^{18}	2.2×10^{18}
VB effective density of state (cm^{-3})	1.8×10^{19}	2.2×10^{16}	1×10^{19}	3.1×10^{18}	1.8×10^{19}	1.8×10^{19}	1.8×10^{19}	1.8×10^{19}	1.8×10^{19}	1.8×10^{19}
electron mobility ($cm^2/(V\ s)$)	20	20	100	974	30	22	16	11	60	145
hole mobility ($cm^2/(V\ s)$)	10	10	25	213	10	22	16	11	20	40
donor density N_D (cm^{-3})	1×10^{17}	1×10^{16}	1×10^{16}							
acceptor density N_A (cm^{-3})				1×10^{19}	1×10^{15}	1×10^{18}	1×10^{18}	1×10^{16}	1×10^{18}	1×10^{18}

Table 3. Simulated PSC Structure Additional Parameters Used in SCAPS-1D

parameters	$CsSnGeI_3$	HTLs	ETLs
N_t value	1×10^{14}	1×10^{15}	1×10^{15}
N_t type	neutral	neutral	neutral
capture cross section (holes)	1×10^{-15}	1×10^{-15}	1×10^{-15}
capture cross section (electrons)	1×10^{-15}	1×10^{-15}	1×10^{-15}
energetic distribution (eV)	Gaussian	single	single
characteristic energy (eV)	0.1	0.1	0.1
energy level w.r.t reference (eV)	0.6	0.6	0.6

large band gap and unique optoelectronic properties. The kesterite HTLs used have been priorly employed as absorbers in thin-film PVs and are viable candidates to be employed as HTLs in PSCs due to their outstanding conductive behavior.[13] A total of 18 PSCs are simulated and optimized in SCAPS-1D employing CTLs contrasting with the $CsSnGeI_3$ absorber layer under standard testing conditions (STCs). Moreover, the impact of CTLs on the electric field, energy band alignment, recombination rate, quantum efficiency (QE), and light absorption is studied carefully. Furthermore, the effects of defect density (N_t), interface defects (ETL/$CsSnGeI_3$ and $CsSnGeI_3$/HTL), temperature (K), and work function (⌀) on the performance of the PSCs are presented in detail.

2. DEVICE MODELING, ARCHITECTURE, AND SIMULATED PARAMETERS OF PSCS

All of the PSCs simulated and modeled in this research work are planar (n-i-p) architectures as shown in Figure 2. It means that light falls first on ETL and passes through it to the $CsSnGeI_3$

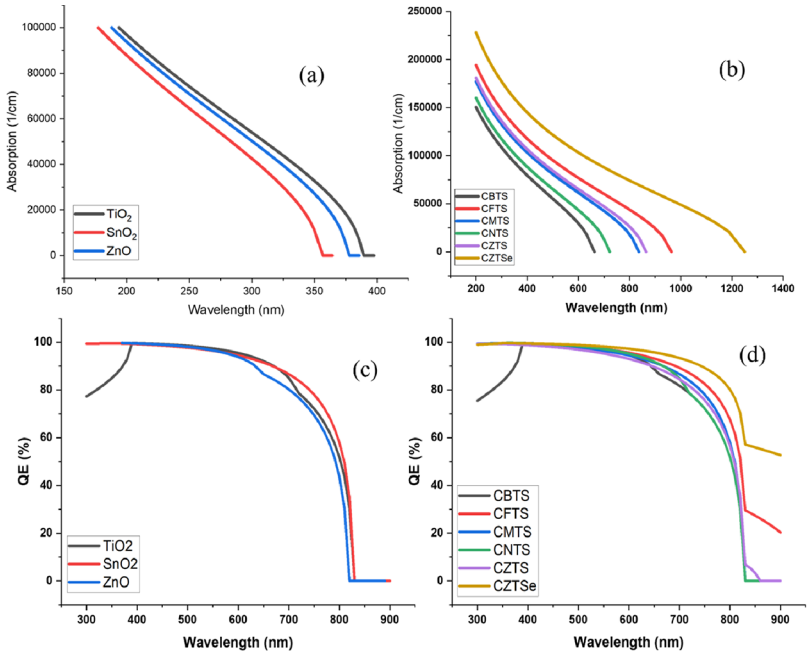

Figure 4. Effect of CTLs on (a, b) the light absorption range and (c, d) QE.

https://doi.org/10.1021/acsomega.3c07754
ACS Omega 2024, 9, 11398−11417

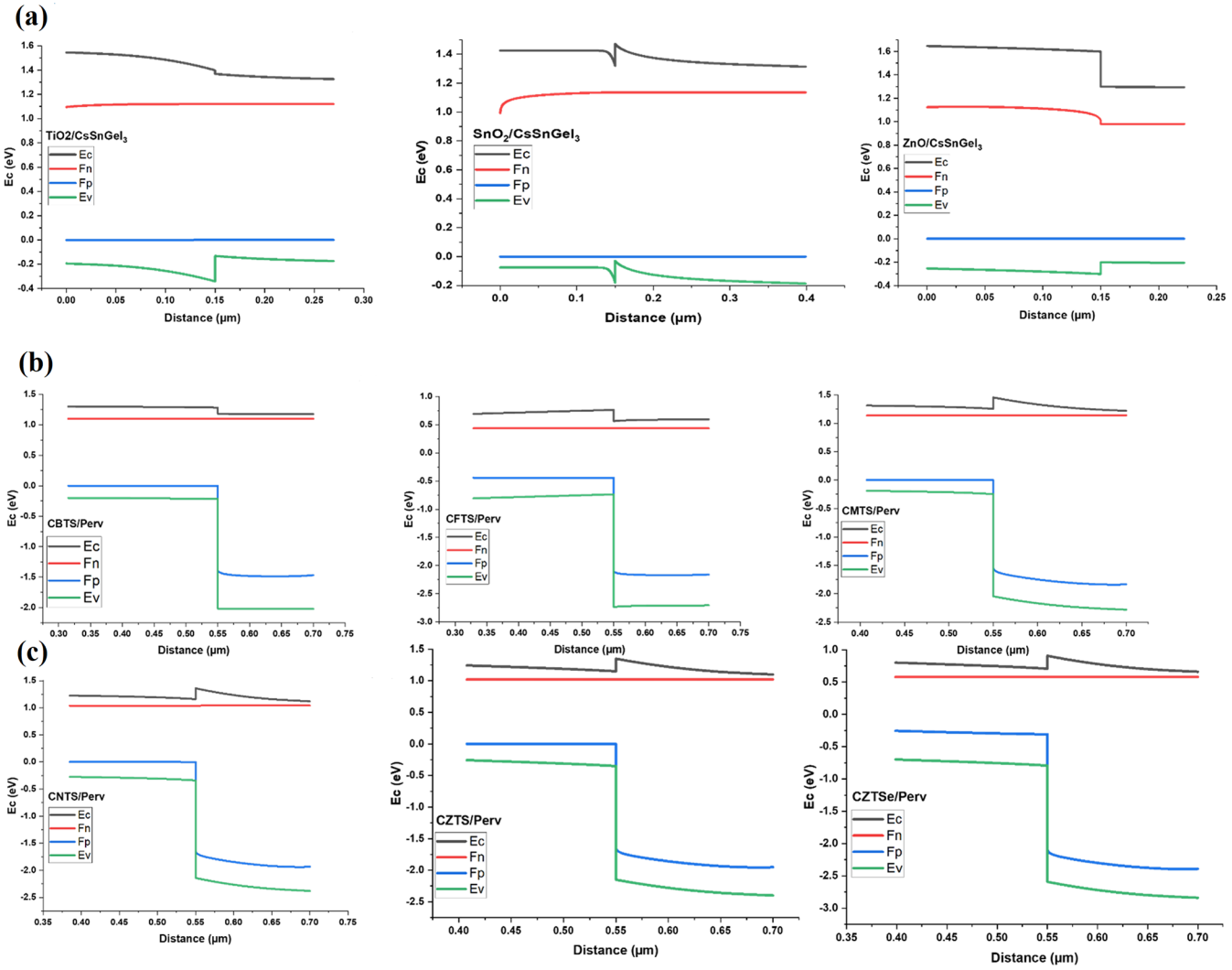

Figure 5. Band alignment of the $CsSnGeI_3$ perovskite layer with (a) ETLs and (b−c) HTLs.

Table 4. CBO and VBO at the ETL/$CsSnGeI_3$ Interface

Interface	CBO (eV)	VBO (eV)
	ETL/Perv	
TiO_2/Perv	−0.1 (cliff)	1.8
SnO_2/Perv	−0.1 (cliff)	2.1
ZnO/Perv	−0.2 (cliff)	2
	Perv/HTL	
Perv/CBTS	0.3	0.1 (spike)
Perv/CFTS	0.6	−0.8 (cliff)
Perv/CMTS	−0.45	0.45 (spike)
Perv/CNTS	0.03	0.21 (spike)
Perv/CZTS	−0.6	0.55 (spike)
Perv/CZTSe	−0.3	−0.2 (cliff)

Table 5. Change in the Recombination Rate at the Heterojunction

interface	recombination rate	rise/drop
Per/TiO_2	1×10^4	drop
Per/SnO_2	1×10^4	drop
Per/ZnO	1×10^3	drop
CBTS/Per	1×10^5	drop
CFTS/Per	1×10^3	rise
CMTS/Per	1×10^6	drop
CNTS/Per	1×10^3	drop
CZTSe/Per	1×10^2	drop
CZTS/Per	1×10^4	drop

layer and then onward to the HTL. The $CsSnGeI_3$ perovskite layer is positioned between the CTLs. For high performance, charge carriers are required to be properly separated from the absorber and transported to the anode and cathode by the CTLs. The HTL is connected to the anode, and the ETL is connected to the cathode. When light passes through the ETL, it is absorbed by the $CsSnGeI_3$ layer, and charges of opposite polarity are created in it. The HTL extracts the holes from the absorber, and electrons are extracted by the ETL. The charge carriers are then transported to the respective electrodes, and thus, the energy from sunlight is converted into electrical energy. The conduction band (CB) of the perovskite and the ETL should align more closely for optimal energy band alignment of the PSC to promote the transfer of electrons, which is depicted in Figure 3, while the valence band (VB) of the HTL and the absorber should be in close proximity to one another to promote the passage of holes.

SCAPS-1D is PV cell simulator software created at the University of Gent, Belgium. It has the capability to simulate up

https://doi.org/10.1021/acsomega.3c07754
ACS Omega 2024, 9, 11398−11417

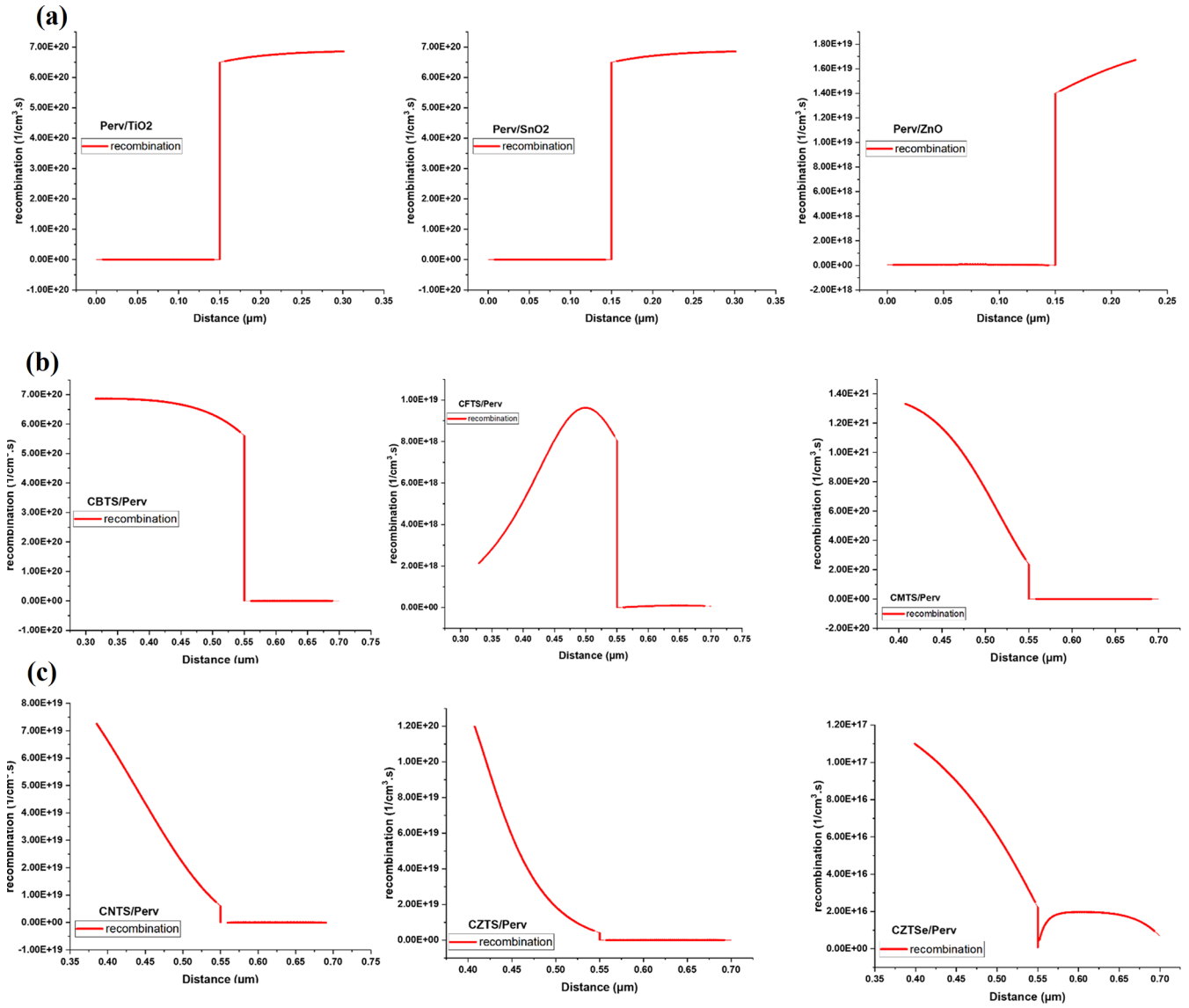

Figure 6. Recombination at the $CsSnGeI_3$ interface with (a) ETLs and (b, c) HTLs.

to seven PSC layers.[20,21] The software is employed in this research work to model, optimize, and investigate various effects on 18 novel PSCs. The perovskite layer chosen is Pb-free "$CsSnGeI_3$", whereas the three ETLs selected are metal oxides (TiO_2, SnO_2, and ZnO), and the HTLs chosen are six quaternary kesterite semiconductor materials (CBTS, CFTS, CNTS, CMTS, CZTS, and CZTSe). Table 1 shows three PSC groups formed having the same kesterite HTLs but contrasting metal oxide ETLs in each group. Each group has six PSC structures, with a total of 18 PSCs modeled and optimized to enhance their PCE. The electrode material is selected as "Flat bands". The software SCAPS-1D simulates the PSC structures under STC using the following equations.[12,13]

Poisson's differential equation

$$\frac{\partial^2 \varphi}{\partial^2 x} = -\frac{\partial E}{\partial x} = -\frac{\rho}{\varepsilon_s} = -\frac{q}{\varepsilon_s}[p - n + N_D(x) - N_A(x) \pm N_{def}(x)] \quad (1)$$

Continuity differential equation

$$\frac{\partial n, p}{\partial t} = \frac{1}{q}\frac{\partial J_n}{\partial x} + (G_n - R_n) + \frac{1}{q}\frac{\partial J_p}{\partial x} + (G_p - R_p) \quad (2)$$

Open-circuit voltage

$$V_{OC} = \frac{nK_BT}{q}\left[\ln\left(\frac{I_L}{I_O} + 1\right)\right] \quad (3)$$

Absorption

$$(\alpha \times h\nu)^{1/\gamma} = B(h\nu - E_g) \quad (4)$$

Quantum efficiency

$$QE = \frac{\text{number of charge carriers collected}}{\text{number of photons absorbed}} \quad (5)$$

Electric field

$$E = \sqrt{\left(\frac{2V_{bi}}{\varepsilon}\right)\left(\frac{N_A + N_D}{N_A N_D}\right)} \quad (6)$$

Recombination rate

https://doi.org/10.1021/acsomega.3c07754
ACS Omega 2024, 9, 11398−11417

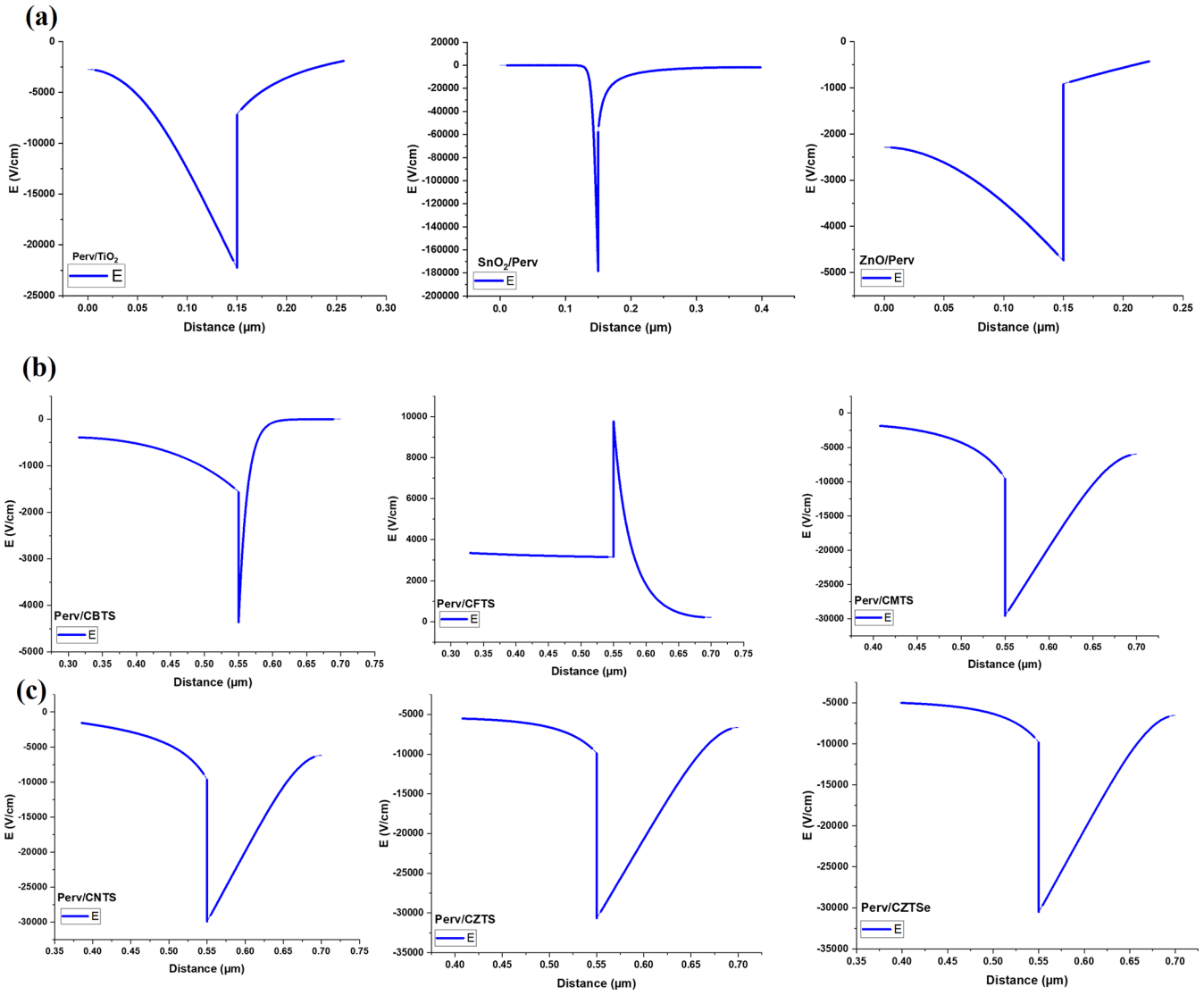

Figure 7. Electric field at the $CsSnGeI_3$ interface with (a) ETLs and (b, c) HTLs.

$$R = \frac{np - n_i^2}{\tau_n(p + p_1)\tau_p(n + n_1)} \tag{7}$$

Transport equation

$$J_{n,p} = nq\mu_n E + qD_n\frac{\partial n}{\partial x} + pq\mu_p E + qD_p\frac{\partial p}{\partial x} \tag{8}$$

Diffusion length

$$L_{n,p} = \sqrt{D_{n,p}\tau_{n,p}} \tag{9}$$

Diffusivity

$$D_{n,p} = \left[\left(\frac{K_B T}{q}\right)\mu_{n,p}\right] \tag{10}$$

Carrier lifetime

$$\tau = \frac{1}{\sigma \times N_t \times V_{th}} \tag{11}$$

Here, φ is the electrostatic potential of the cell; E is the electric field; ρ and q are the elementary charges; ε is the permittivity of the material; n is the free electron/hole density; p, n_1, and p_1 are the electron and hole densities at thermal equilibrium; N_A (acceptor) and N_D (donor) are the doping densities; $\mu_{n,p}$ is the electron/hole mobility; $\tau_{n,p}$ is the electron/hole lifetime; $\frac{\partial n,p}{\partial x}$ is the electron/hole concentration gradient; $G_{n,p}$ is the optical generation rate; $R_{n,p}$ is the recombination rate; $\frac{K_B T}{q}$ is the thermal voltage; I_L is the light generated current; I_O is the saturation current; α represents the absorption coefficient of the material; the Plank constant is represented by h; the photon frequency is denoted by v; the direct/indirect transition is presented by γ; and B is a constant.

In this research work, the simulated parameters for the $CsSnGeI_3$ perovskite, metal oxide ETLs, and kesterite HTLs used in SCAPS-1D have been taken from various research papers[12−15] and are summarized in Table 2. In the perovskite layer, the main defects are the crystal structure deformities and the trap states, which hinder the transportation of the charge carriers. For this reason, the defect density in the perovskite is selected as neutral.[22] Moreover, the energetic distribution is kept as Gaussian type with a characteristic energy of 0.1 eV and a capture cross-section area of 2×10^{-14} cm^2. While for the defects in the CTL, only the trap states in the layers are considered.

https://doi.org/10.1021/acsomega.3c07754
ACS Omega 2024, 9, 11398−11417

Table 6. Output Electrical Characteristics of Simulated Nonoptimized PSC Structures

s.no.	PSC structures	J_{sc} (mA/cm^2)	V_{oc} (V)	FF%	PCE%
1	TiO_2/$CsSnGeI_3$/CBTS	24.49294	1.0969	83.81	22.52
2	TiO_2/$CsSnGeI_3$/CFTS	27.38856	0.4337	77.57	9.21
3	TiO_2/$CsSnGeI_3$/CMTS	24.11754	1.1194	44.27	11.95
4	TiO_2/$CsSnGeI_3$/CNTS	24.77125	1.1101	86.97	23.92
5	TiO_2/$CsSnGeI_3$/CZTS	17.19194	1.5492	25.59	6.82
6	TiO_2/$CsSnGeI_3$/CZTSe	24.11298	0.7494	83.74	15.13
7	SnO_2/$CsSnGeI_3$/CBTS	24.62038	0.901014	78.0427	17.3125
8	SnO_2/$CsSnGeI_3$/CFTS	27.49972	0.36	72.7418	7.2014
9	SnO_2/$CsSnGeI_3$/CMTS	25.22429	1.123006	87.0006	24.6447
10	SnO_2/$CsSnGeI_3$/CNTS	24.87967	1.030311	82.0173	21.0241
11	SnO_2/$CsSnGeI_3$/CZTS	24.92056	1.017603	85.9362	21.7928
12	SnO_2/$CsSnGeI_3$/CZTSe	35.12103	0.575963	78.0489	15.7881
13	ZnO/$CsSnGeI_3$/CBTS	24.60385	0.9648	84.11	19.97
14	ZnO/$CsSnGeI_3$/CFTS	27.46376	0.4359	77.49	9.28
15	ZnO/$CsSnGeI_3$/CMTS	24.92425	0.9597	41.81	10.00
16	ZnO/$CsSnGeI_3$/CNTS	24.87134	0.9601	82.12	19.61
17	ZnO/$CsSnGeI_3$/CZTS	15.69919	0.9652	38.77	5.88
18	ZnO/$CsSnGeI_3$/CZTSe	24.11474	0.7743	80.1	14.96

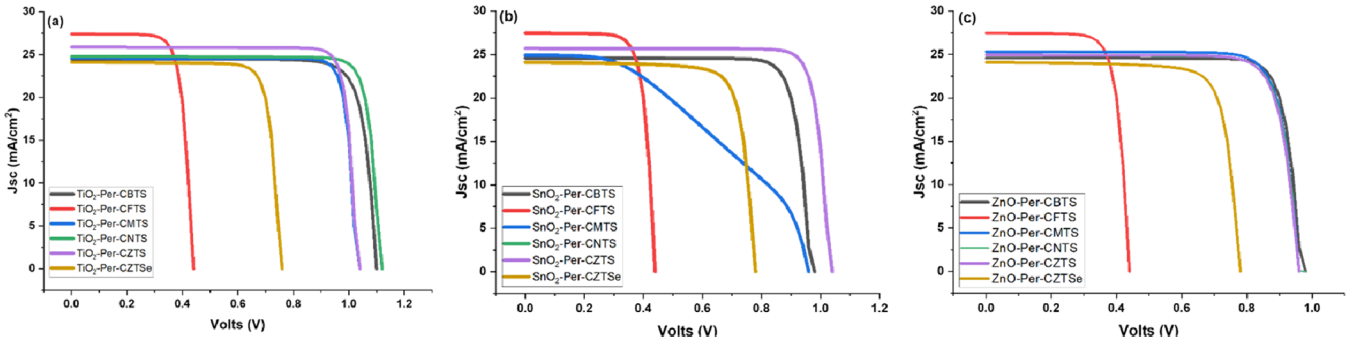

Figure 8. *I*−*V* curves of nonoptimized (a) TiO_2-based structures, (b) SnO_2-based structures, and (c) ZnO-based structures.

Therefore, the defect type is selected as neutral, with energetic distribution as single type.[23] Furthermore, the CTL/perovskite interface defects between the layers are caused by the dangling bonds and defects formed at the surfaces and grain boundaries between the two layers. For both interfaces, the defect type is selected as neutral, with energetic distribution as single type and the defect energy level above the highest valence band.[7] The perovskite and CTLs are modeled with defect density (N_t) and interface defects. The "N_t" for $CsSnGeI_3$ is taken as 1×10^{14} and 1×10^{15} cm^{-3} for CTLs, while it is 1×10^{12} cm^{-3} for both interfaces. Table 3 summarizes the remaining simulation parameters used in SCAPS-1D.

3. RESULTS AND DISCUSSION

3.1. Perovskite and CTL Compatibility. *3.1.1. Light Absorption by CTLs and Their Effect on Quantum Efficiency.* Figure 4a shows the absorption of the light spectrum by the metal oxide ETLs, whereas Figure 4b shows the absorption by the kesterite HTLs. The results show that the maximum light absorption range of TiO_2 is up to 390 nm, whereas for SnO_2 it is up to 355 nm, and for ZnO it is up to 375 nm. Figure 4a shows that the performance of $Sn0_2$-based structures is higher because of its lower absorption rate owing to the high band gap, which gives the material more transmissivity compared to the other two ETLs (TiO_2 and ZnO). Hence, maximum light is transmitted by it to be absorbed by the $CsSnGeI_3$ absorber layer. The ETL in the planar architecture needs to have low optical absorption, as it is the front layer upon which the incident light is to fall upon. Maximum transmissivity is helpful in enhancing the PCE.[29] Figure 4b shows the absorption spectrum of the kesterite HTLs ranges between 670 and 1290 nm due to their varying E_g values, and among the HTLs, CBTS has the lowest optical absorption of less than 680 nm due to its high E_g value of 1.9 eV, followed by CNTS (1.74 eV) and CMTS (1.5 eV), whereas HTLs having low E_g values like CZTSe (1.0 eV) and CFTS (1.3 eV) have a high absorption coefficient at greater wavelengths.[30]

Figure 4c,d shows the effect of CTLs on the QE of the PSCs. TiO_2 has a QE of 99.64% at 360 nm, whereas that of SnO_2 is 99.53% at 350−360 nm, while that of ZnO is 99.70% at 380 nm. The QE of CTLs tends to drop as the wavelength starts to increase. Furthermore, among the HTLs, the QE of CBTS is 99.62% at 380 nm, CFTS is 99.58% at 380 nm, CMTS is 99.53% at 360 nm, CNTS is 99.74% at 360 nm, CZTS is 99.34% at 320 nm, and CZTSe is 99.64% at 360 nm.

3.1.2. Energy Band Alignment of CTLs with $CsSnGeI_3$. The band alignment among the absorber layer, ETL, and HTL is very crucial for efficient charge transfer to the electrodes.[10,31,32] A PSC produces charge carriers when light strikes it. The CB of the perovskite should be aligned with the ETL's CB to provide a smooth flow of electrons to the cathode, and the VB of the perovskite should be aligned with the HTL's VB to facilitate the flow of holes to the anode. Therefore, the right selection of CTLs is necessary to achieve the desired band alignment. The

https://doi.org/10.1021/acsomega.3c07754
ACS Omega 2024, 9, 11398−11417

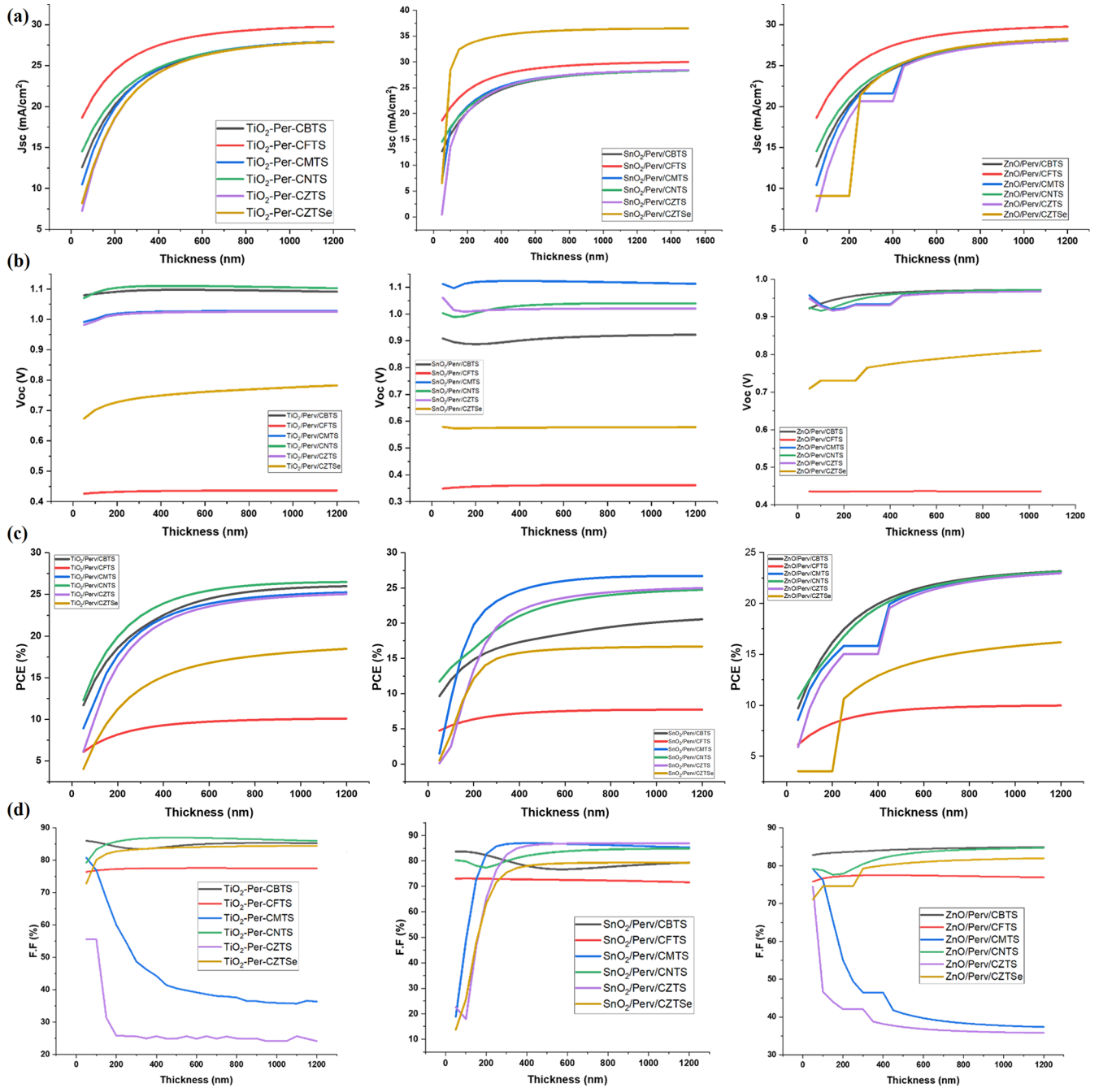

Figure 9. $CsSnGeI_3$ thickness effect on (a) J_{sc}, (b) V_{oc}, (c) PCE, and (d) FF of PSCs.

band alignment is also affected by the doping concentration of the CTL materials. In PSCs, a positive conduction band offset (+CBO) or spike is formed when the CB of the absorber is lower than the ETL's CB, while a cliff or negative CBO is formed when the perovskite CB is higher than the ETL's CBA; +CBO is recommended instead of −CBO to facilitate the flow of electrons because the spike increases the internal electric potential (V_{bi}) of a cell at the heterojunction. This results in a better separation of the charge carriers. However, very large spikes (greater than 0.3 eV) also cause the blockage of charge carriers, thus reducing the transfer of charge carriers. The cliff (negative band offset) reduces the potential, leading to lower charge carriers being affected. Therefore, it is preferred to have a band offset between 0 and 0.3 eV. Similarly, for holes to flow easily toward the anode, the positive valence band offset (+VBO) is recommended instead of −VBO as it increases the V_{bi} of the cell and improves the overall performance.[13] The ETLs that form large VBO with the perovskites help in blocking hole transfer toward the cathode and in maximizing the PCE. However, the HTL that forms a large CBO with the perovskites helps in blocking electron transfer to the anode. To improve the PCE of PSCs, it is important to have such a band alignment between the various CTLs and the perovskite layer to ensure maximum performance. The CBO and VBO of the CTL with the perovskite material can be calculated by the following equations[7]

$$\mathrm{CBO} = (\chi_{per} - \chi_{CTL}) \tag{12}$$

https://doi.org/10.1021/acsomega.3c07754
ACS Omega 2024, 9, 11398−11417

Table 7. Output Electrical Characteristics of Simulated Optimized PSC Structures

PSCs	perovskite thickness (nm)	HTL thickness (nm)	ETL thickness (nm)	perovskite doping cm^{-3}	ETL doping cm^{-3}	HTL doping cm^{-3}	J_{SC} (mA/cm^2)	V_{oc} (V)	FF %	PCE (%)
TiO_2/$CsSnGeI_3$/CBTS	1100	150	100	1×10^{14}	1×10^{15}	1×10^{19}	27.93	1.05	82.70	24.35
TiO_2/$CsSnGeI_3$/CFTS	750	250	100	1×10^{15}	1×10^{16}	1×10^{20}	29.98	0.55	81.49	13.49
TiO_2/$CsSnGeI_3$/CMTS	300	250	100	1×10^{17}	1×10^{20}	1×10^{20}	22.08	1.13	89.05	22.37
TiO_2/$CsSnGeI_3$/CNTS	1000	100	100	1×10^{15}	1×10^{20}	1×10^{18}	27.69	1.15	84.97	27.21
TiO_2/ $CsSnGeI_3$/CZTS	250	300	100	1×10^{12}	1×10^{20}	1×10^{20}	20.56	1.13	88.48	20.74
TiO_2/$CsSnGeI_3$/CZTSe	1200	100	100	1×10^{16}	1×10^{20}	1×10^{20}	27.38	0.95	85.22	22.17
SnO_2/$CsSnGeI_3$/CBTS	1200	150	100	1×10^{15}	1×10^{17}	1×10^{20}	28.05	1.12	86.13	27.13
SnO_2/ $CsSnGeI_3$/CFTS	600	300	100	1×10^{12}	1×10^{18}	1×10^{19}	29.99	0.36	75.38	8.19
SnO_2/Per/CMTS	900	150	100	1×10^{12}	1×10^{18}	1×10^{20}	27.69	1.16	84.85	27.30
SnO_2/Per/CNTS	1200	100	100	1×10^{15}	1×10^{18}	1×10^{20}	28.04	1.14	85.00	27.33
SnO_2/Per/CZTS	1100	150	100	1×10^{12}	1×10^{18}	1×10^{20}	28.08	1.12	86.36	27.17
SnO_2/Per/CZTSe	700	300	100	1×10^{12}	1×10^{18}	1×10^{20}	39.48	0.70	84.48	23.50
ZnO/Per/CBTS	1200	100	100	1×10^{12}	1×10^{20}	1×10^{15}	28.02	1.10	84.63	26.27
ZnO/$CsSnGeI_3$/CFTS	700	300	100	1×10^{15}	1×10^{18}	1×10^{20}	30.19	0.55	81.66	13.63
ZnO/$CsSnGeI_3$CMTS	600	250	100	1×10^{17}	1×10^{15}	1×10^{20}	26.33	1.00	87.52	23.28
ZnO/$CsSnGeI_3$/CNTS	1200	100	100	1×10^{12}	1×10^{20}	1×10^{17}	28.01	1.13	84.91	27.02
ZnO/$CsSnGeI_3$/CZTS	200	250	100	1×10^{15}	1×10^{15}	1×10^{20}	18.65	0.93	83.97	14.63
ZnO/$CsSnGeI_3$/CZTSe	1200	100	100	1×10^{15}	1×10^{19}	1×10^{20}	27.99	0.90	86.26	21.78

$$\mathrm{VBO} = (\chi_{\mathrm{CTL}} - \chi_{\mathrm{per}} + E_{\mathrm{gCTL}} - E_{\mathrm{gper}}) \quad (13)$$

where E_g is the band gap of the material and χ is the electron affinity.

Figure 5a shows the band alignment at the ETLs/$CsSnGeI_3$ interface, while Table 4 shows their CBO and VBO values. It can be depicted from Table 4 that SnO_2 forms a CBO of −0.1 eV at the interface, which allows the smooth flow of electrons from the $CsSnGeI_3$ perovskite to the SnO_2 and has a high VBO of 2.1 eV to block the flow of holes. Similarly, TiO_2 also forms a CBO of −0.1 eV and forms a minute cliff at the interface and a high CBO of 1.8 eV to block the flow of holes toward it. ZnO forms a CBO of −0.2 eV and forms a higher cliff as compared to the other ETLs and has a VBO of 2 eV. The SnO_2-based Group 2 showed better performance than the other ETLs because it is close to the ideal energy band alignment and has minimal CBO and maximum VBO at the SnO_2/$CsSnGeI_3$ interface.

Figure 5b,c shows the band alignment at the $CsSnGeI_3$/HTLs interface, while Table 5 depicts their CBO and VBO values. It can be seen that CFTS forms a cliff of −0.8 eV at the interface and, as a result, has a comparatively lower performance than the rest of the HTLs, while CNTS outperforms all of the other HTLs because of its preferable VBO of 0.21 eV, forming a spike that boosts the V_{bi} of the cell.

The rest of the HTLs performed comparatively the same in terms of their output performance but have varying band alignments with the $CsSnGeI_3$ perovskite layer. The poor band alignment at the $CsSnGeI_3$/HTL interface hinders the smooth flow of holes from the $CsSnGeI_3$ layer to the HTL and offers less resistance to the recombination of the e−h pair at the interface, thus lowering the V_{oc} of the cell and resulting in a lower PCE.

3.1.3. Recombination Rate at Interfaces (ETL/Perovskite and Perovskite/HTL). The CTLs act as a bridge between the perovskite and electrodes to assist in the passage of charge carriers from the absorber layer. However, the PSC's interfaces (ETL/perovskite and perovskite/HTL) degrade performance as a result of charge carriers' recombination at the junction.[33−35] The charge carriers become trapped in defects at the interfaces and lead to loss of photocurrent, hence reducing the PCE. The two forms of recombination at the interfaces are trap-assisted and direct recombination. The recombination at the interfaces can be reduced by adding a passivation layer between the perovskite and CTLs.

Figure 6a shows the recombination rate at the ETL/$CsSnGeI_3$ interface, and Table 4 shows the CBO and VBO values of the ETLs at this particular interface. The results demonstrate that TiO_2 and SnO_2 have a CBO value of −0.1 eV (cliff), while ZnO has a higher cliff of −0.2 eV. The ETL has VBO values of 1.8, 2.1, and 2 eV, respectively. Due to the formation of a cliff by all three ETLs at the interface, some degree of recombination of charge carriers occurs.

Figure 6b,c depicts the recombination rate at the $CsSnGeI_3$/HTL interface, and Table 4 shows their VBO values, in which it can be seen that CFTS and CZTS have negative VBO (cliff) values of −0.8 and −0.2 eV due to which recombination occurs as compared to the remaining HTLs that form a positive VBO (spike) at the interface. Table 5 shows the change in the recombination rate at the heterojunction of the different materials.

3.1.4. Electric Field at Interfaces. Due to the formation of the heterojunction at the interface of different PSC layers, the electric field is produced. The band alignment plays a significant role in the potential of the field. A spike increases the electric field, while a cliff reduces it.[18,19,36] A strong electric field has a deeper influence on the bulk of the absorber than a weaker field. The stronger electric field collects and separates the deeper-lying photo-generated charge carriers more effectively.

The electric field at the ETL/$CsSnGeI_3$ interface is shown in Figure 7a. The results show that SnO_2 has the highest built-in potential of −180,000 V/cm, followed by TiO_2 having −22,500 V/cm. However, ZnO has the lowest electric potential of −4800 V/cm among the three ETLs due to its large negative CBO of −0.2 eV, which lowers its electric potential at the interface.

On the other hand, Figure 7b,c shows the generated electric field at the $CsSnGeI_3$/HTL interface, and the results from Table 4 show that among all of the HTLs, CFTS forms a very large cliff at the interface, which lowers the electric field due the large negative VBO of −0.8 eV, while the rest of the HTLs form a positive VBO (spike) and increase the electric potential of the HTLs up to −30,000 V/cm.

https://doi.org/10.1021/acsomega.3c07754
ACS Omega 2024, 9, 11398−11417

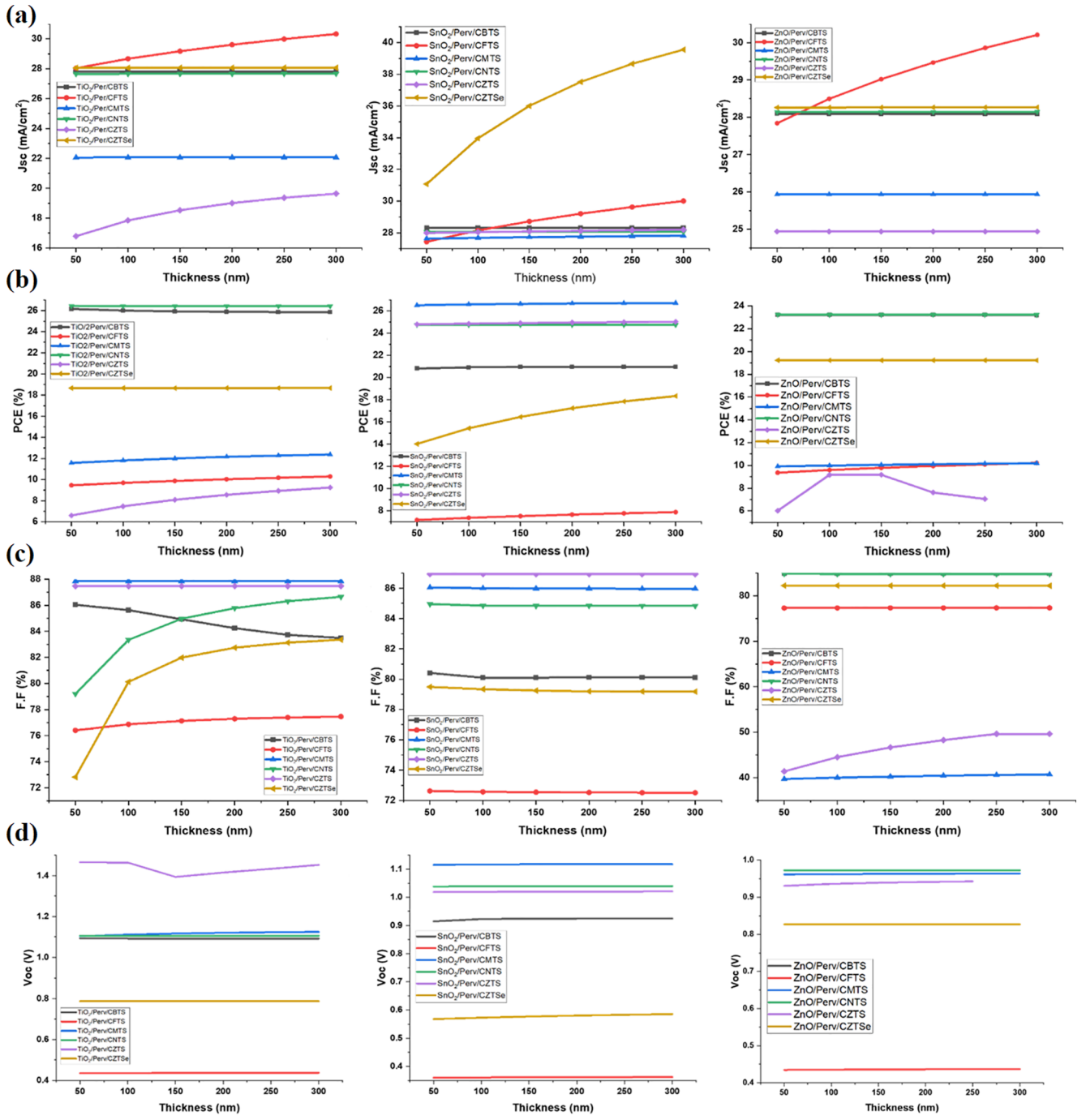

Figure 10. HTL thickness variation effect on (a) J_{sc}, (b) PCE, (c) FF, and (d) V_{oc} of PSCs.

3.2. *I*–*V* Characteristics of Simulated Nonoptimized PSC Structures. Table 6 and Figure 8a–c show the *I*–*V* results of all 18 simulated nonoptimized PSC structures. The outcomes demonstrate that the CTLs have a direct impact on how well the PSC performs. Among the three groups, the SnO_2-based structures (Group B) in general showed better PV performance as compared to its other counterparts because of its large band gap (E_g) (3.5 eV). Similarly, the TiO_2- and ZnO-based structures of Group "A" and Group "C" showed a slightly lower performance as compared to Group "B" structures because of their comparatively smaller E_g values (3.2 and 3.3 eV). Furthermore, among the HTLs, CFTS and CZTS performed the worst as they form negative VBO (cliff) values of −0.8 and −0.2 eV, respectively, at the $CsSnGeI_3$–HTL interface, while the other four HTLs performed comparatively better because they form a positive VBO (spike) at the interface as shown in Table 4. The most efficient nonoptimized PSC among all 18 structures is SnO_2/$CsSnGeI_3$/CMTS with a J_{sc} of 25.22 mA/cm^2, V_{oc} of 1.12 V, FF of 87%, and PCE of 24.67%, while the least efficient PSC structure is ZnO/$CsSnGeI_3$/CZTS with a J_{sc} of 15.69 mA/cm^2, V_{oc} of 0.96 V, FF of 38.77%, and PCE of 5.88%.

3.3. Thickness Optimization of the $CsSnGeI_3$ Perovskite Layer. The thickness of the perovskite layer is an important factor in determining the PCE, charge transport, and stability of the PSC. To design an efficient and stable PSC, the

https://doi.org/10.1021/acsomega.3c07754
ACS Omega 2024, 9, 11398−11417

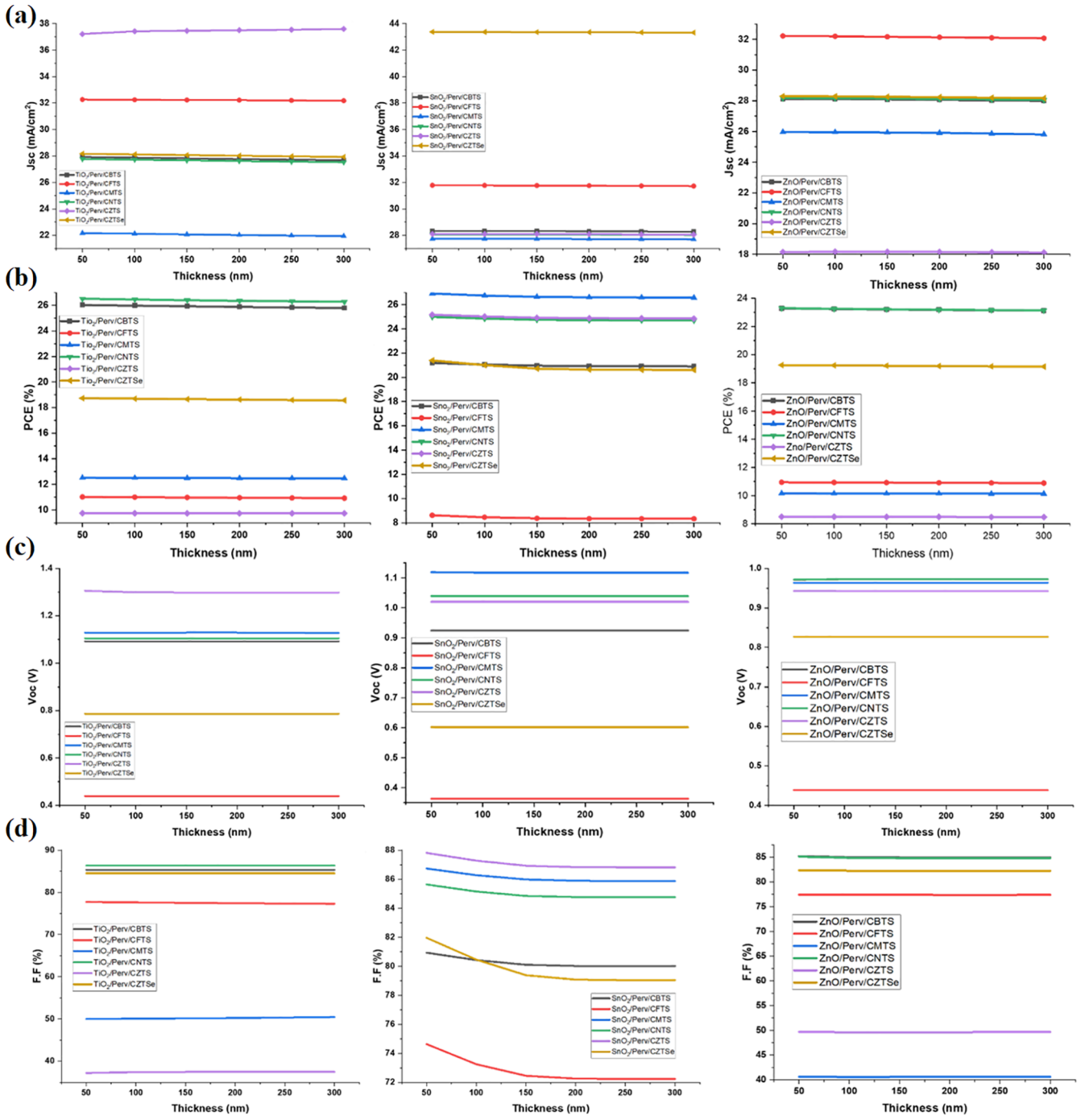

Figure 11. Impact of ETL thickness variation on the (a) J_{sc}, (b) PCE, (c) V_{oc}, and (d) FF of PSCs.

optimal thickness of the absorber layer needs to be known, as neither a thicker nor a very thin layer is recommended for the designing of efficient PSCs. In a thick absorber, although more light is absorbed, there are chances of increased recombination, affecting the performance of the PSC. Furthermore, in a thin absorber layer, minimum light is absorbed and fewer charge carriers are generated. Moreover, the perovskite layer is prone to degradation so there needs to be a balance between compromising stability and efficiency of the PSC.[12,37−39]

In this study, the $CsSnGeI_3$ layer thickness is optimized for all 18 PSCs by altering it between 50 and 1200 nm with an increment of 50 nm to determine the absorber's ideal thickness. Figure 9a−d shows the simulation results of how the J_{sc}, V_{oc}, PCE, and FF of the PSCs are influenced due to increasing $CsSnGeI_3$ layer thickness. The FFs of all of the structures except for CMTS and CZTS structures in Groups 1 and 3 have less optimal absorber thicknesses as their FFs decrease with increased $CsSnGeI_3$ thickness. The outcomes demonstrate that raising the $CsSnGeI_3$ thickness is beneficial in improving the output performance of all of the PSCs. It is because due to the increased thickness, the ability of the perovskite layer to absorb more photons was enhanced. As more photons are absorbed by the thick $CsSnGeI_3$ layer, the $I-V$ characteristics improve as a result. It is also noteworthy that using a very thick or a very thin absorber layer is ineffective. Therefore, to enhance the PCE of the cell, an optimized value of absorber thickness is a very crucial

https://doi.org/10.1021/acsomega.3c07754
ACS Omega 2024, 9, 11398−11417

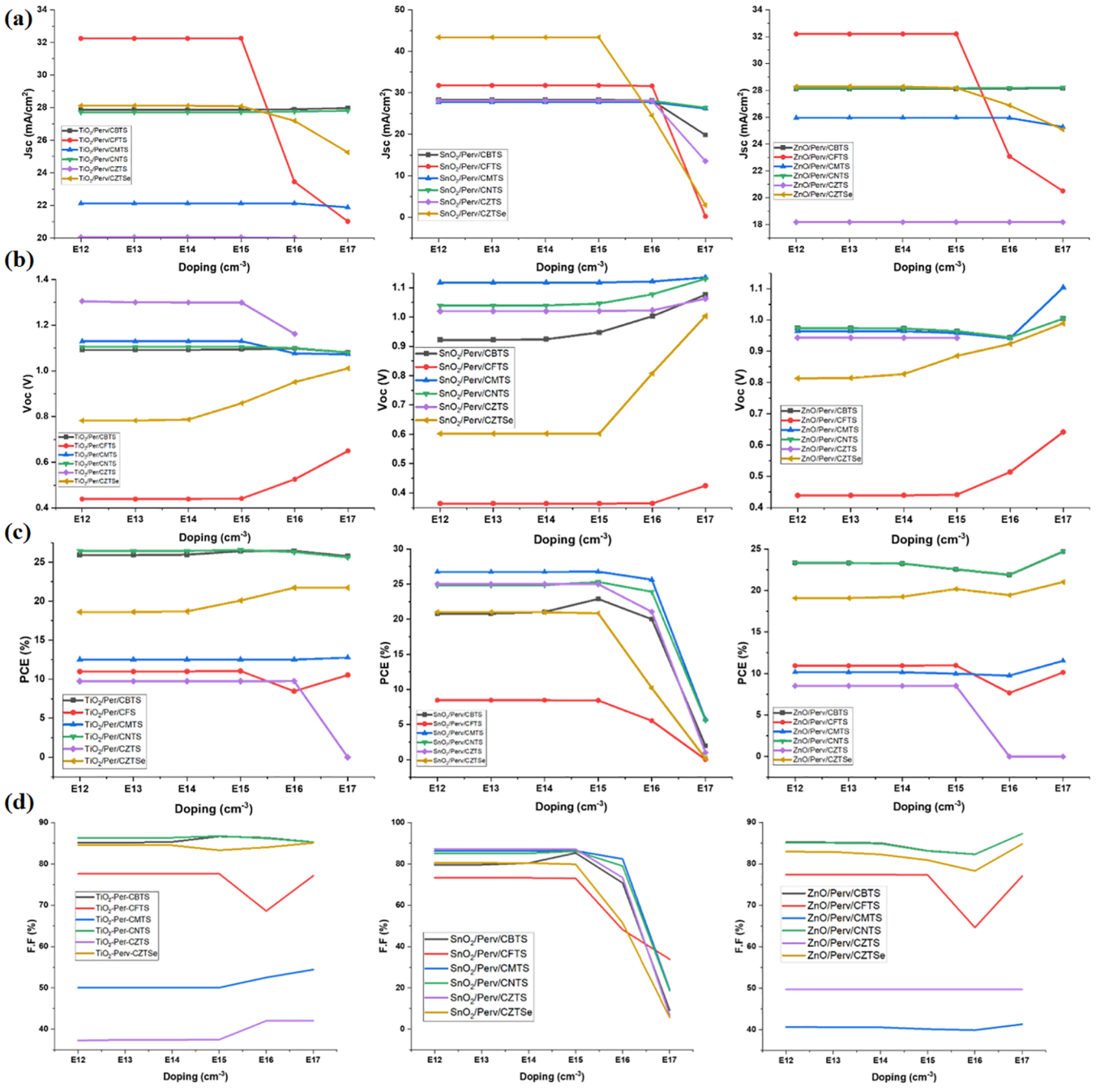

Figure 12. $CsSnGeI_3$ doping effect on (a) J_{sc}, (b) V_{oc}, (c) PCE, and (d) FF of PSCs.

factor. The value of the optimized thickness for each individual structure is presented in Table 7, which observes the cell's $I-V$ results for every 50 nm increase in thickness. Once the optimized thickness is achieved, the PCEs of the cells do not improve with a further increase in the absorber layer thickness.

3.4. Kesterite HTL Thickness Optimization. In the PSC architecture, the HTL is positioned between the perovskite and the anode. The HTL thickness influences the performance of the PSC as it is the rear layer in the n-i-p architecture and may absorb the remaining passed-out light from the absorber. In order to provide proper hole separation and minimize recombination at the HTL/perovskite contact, the HTL should be of a reasonable thickness. In the PSC architecture, neither a thick nor a thin HTL is advised because it compromises the cell's functionality and stability.[19,25] The HTL thickness optimization is the second step after finding the optimal thickness of the absorber layer.

In this work, the HTL thickness in each structure was varied from 50 to 300 nm to find the optimal thickness. The performance of the PSCs was carefully monitored for thickness increase by 50 nm increments. The results show that increasing the HTL thickness did not have a significant effect on the PCE of the PSCs. For all 18 structures, the ideal HTL thickness ranged from 100 to 300 nm. Figure 10a shows that the J_{sc} of PSCs either stays constant or improves with increased HTL thickness.

Similarly, Figure 10b shows the impact of HTL thickness on the PCE of the cells, and it shows that increasing the HTL thickness did not have a significant impact on enhancing the PCE of all of the group structures except for $TiO_2-CsSnGeI_3-CZTSe$ and $SnO_2-CsSnGeI_3-CZTS$, whose PCE improved up

https://doi.org/10.1021/acsomega.3c07754
ACS Omega 2024, 9, 11398−11417

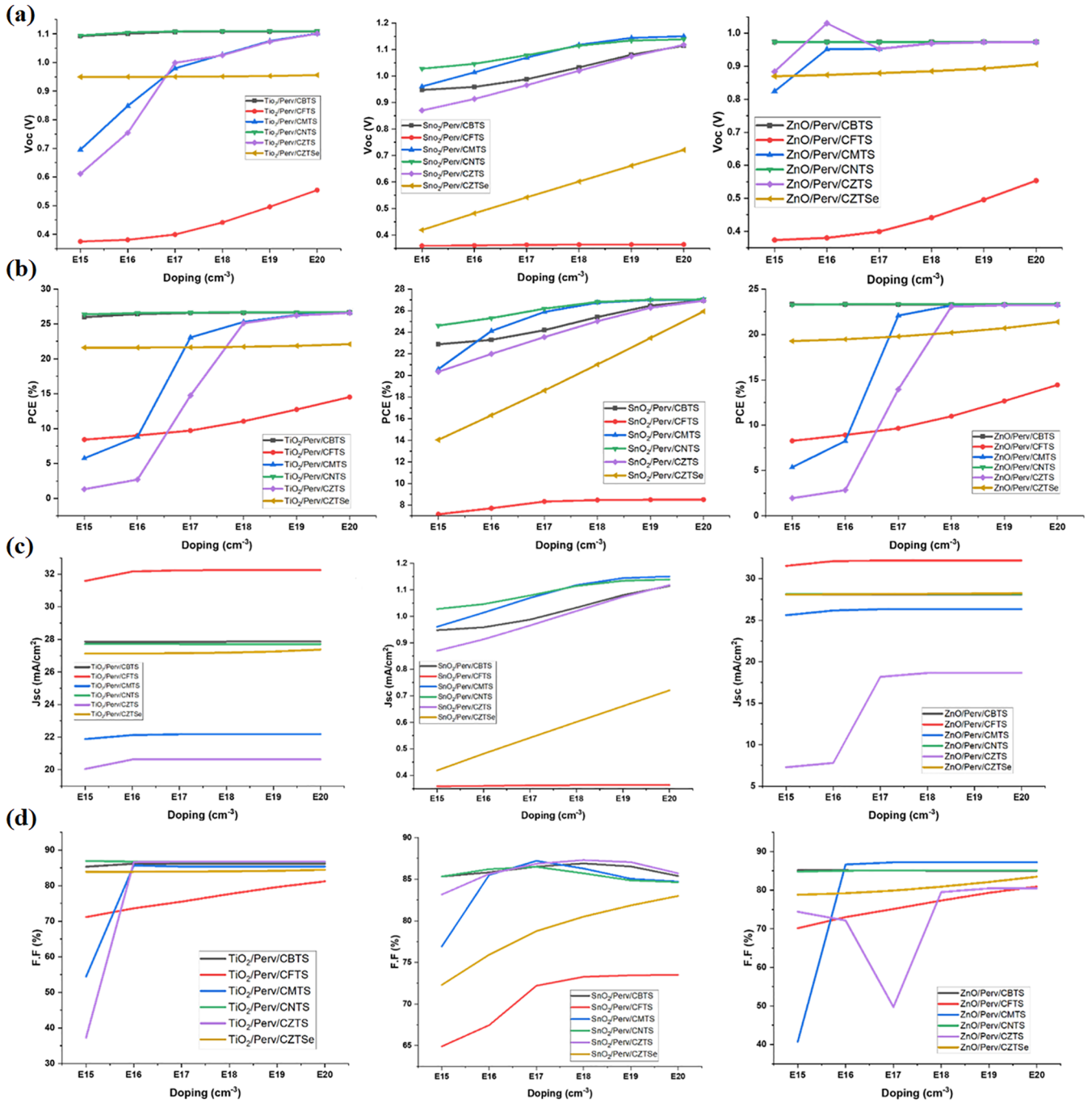

Figure 13. HTL doping effect on (a) V_{oc}, (b) PCE, (c) J_{sc}, and (d) FF of PSCs.

to 5%. Figure 10c shows the impact of HTL thickness on the FFs of all of the structures, and it can be seen that in Group A, the FF of the structures with CFTS, CNTS, and CZTSe saw an increase, while that of the CBTS degraded, respectively, whereas all of the structures in Groups B and C showed a constant run except for ZnO-$CsSnGeI_3$−CZTS, whose FF improved on increasing the HTL thickness. Table 7 shows the optimized value of the HTL thickness for all of the simulated structures.

3.5. Metal Oxide ETL Thickness Optimization. The ETL is positioned between the cathode and the perovskite in a planar PSC architecture. The incident light first falls on the ETL through which it passes to reach the absorber. The ETL is responsible for the adequate separation and transportation of electrons and thus reduces the recombination rate.[18,25,32] Using a thick ETL reduces the PCE as light might be absorbed by the material. The optimization of the ETL thickness is the third step in optimization of the PSC.

Figure 11a−d shows the effect of ETL thickness on PSC performance. The thickness was varied from 50 to 300 nm for each structure with an increase of 50 nm increment. The results reveal that increasing the ETL thickness does not enhance the $I-V$ performance of the PSCs. Using a thick ETL in the proposed planar PSC architectures is inefficient and increases the series resistance and fabrication cost of the cell. It is recommended to use a transmissive ETL with less optical absorption in the n-i-p architecture to enhance the performance results of the PSC. Table 7 shows that the optimized value of ETL thickness is 100 nm.

https://doi.org/10.1021/acsomega.3c07754
ACS Omega 2024, 9, 11398−11417

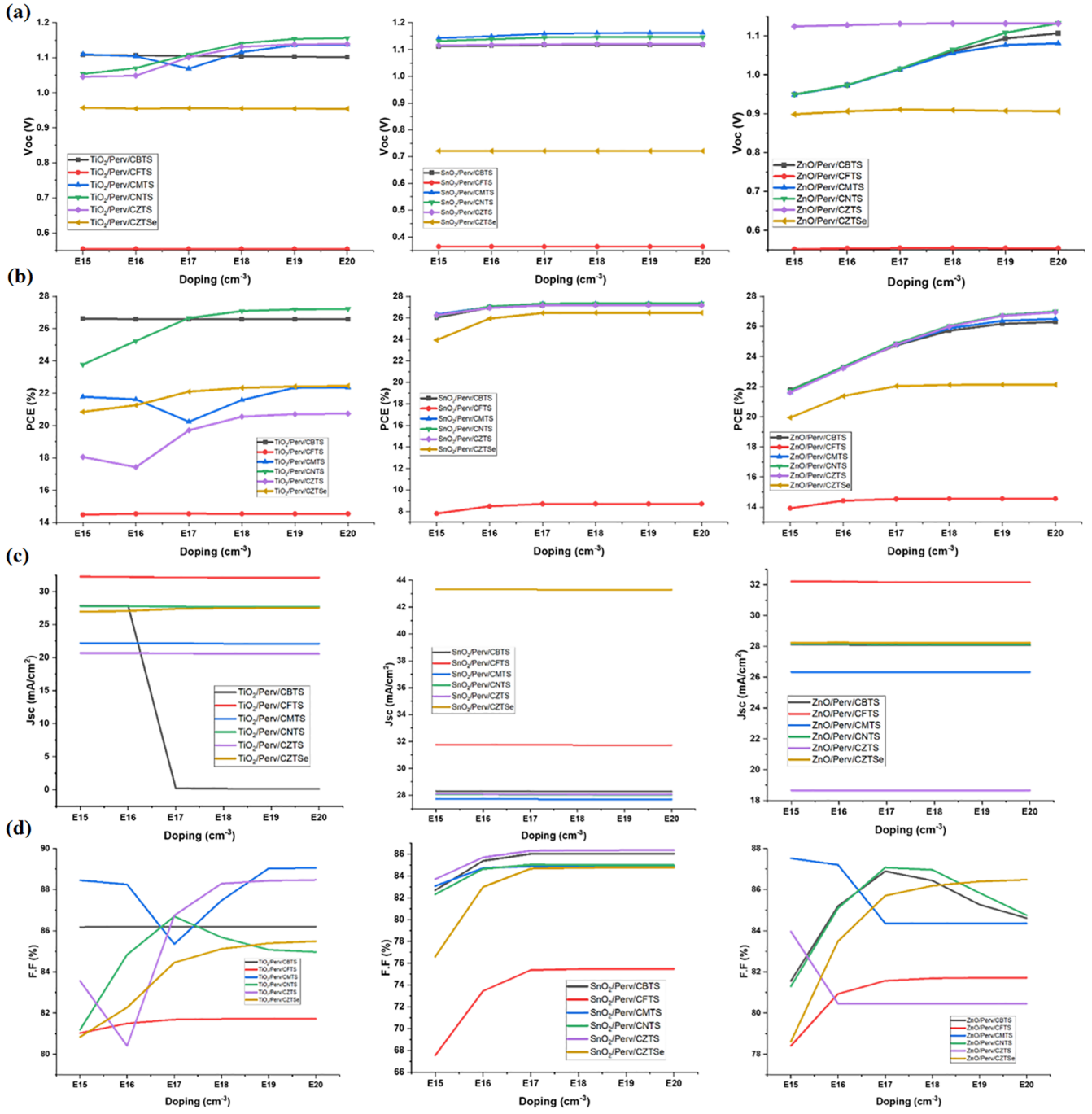

Figure 14. ETL doping variation impact on (a) V_{oc}, (b) PCE, (c) J_{sc}, and (d) FF of PSCs.

3.6. Optimization of the Doping Concentration of the $CsSnGeI_3$ Perovskite Layer. The doping concentration (N_A) of the absorber has a significant impact on the electronic properties and stability of the PSC.[17,19,40] Low doping concentration has a negligible effect on the performance of the PSC, and high doping leads to defects and degradation. Therefore, it is vital to find the optimized doping concentration to enhance the performance of the PSC without compromising its electronic properties and stability. Optimizing the N_A is the fourth step in the device optimization of the PSC.

Figure 12a–d shows the impact of varying the doping percentage of the absorber layer in each PSC structure from 1×10^{12} to 1×10^{17} cm^{-3}. The results obtained in all three groups show that the $I-V$ performance was not affected by the N_A of 1×10^{15} cm^{-3}. Further increase has a significant impact on the PCE of most of the structures as it starts to degrade. The optimized doping concentration for the $CsSnGeI_3$ perovskite layer in each structure was found between 1×10^{12} and 1×10^{15} cm^{-3}, and the results are summarized in Table 7. The J_{sc} of all of the structures showed a downward trend, whereas the V_{oc} and FF of some structures showed a slight improvement, but the overall PCE of the structures was negatively affected by the increased doping content of the $CsSnGeI_3$ absorber layer.

3.7. Doping Optimization of Kesterite HTLs. The doping of HTL affects the electronic properties, work function, conductivity, stability, and performance of the PSC. From the active layer to the electrode, holes must be transported via the HTL. The ion separation process is facilitated by the doping of

https://doi.org/10.1021/acsomega.3c07754
ACS Omega 2024, 9, 11398−11417

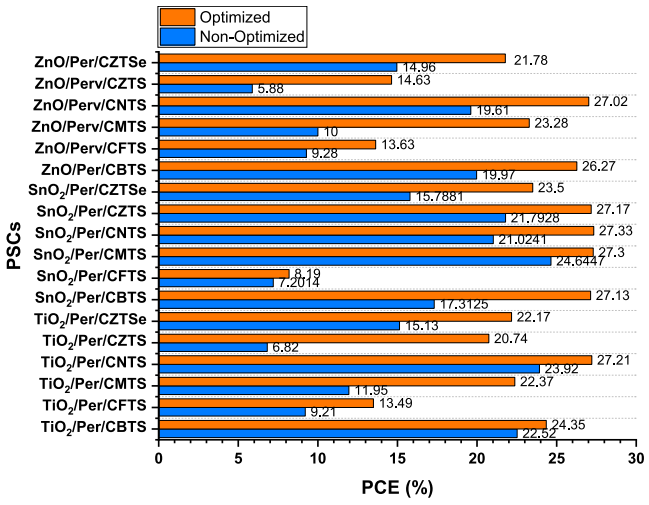

Figure 15. PCE results before and after optimization.

the HTL, which also enhances the material conductivity.[27,39,41] The doping optimization is the fifth step in device optimization.

Figure 13a,b demonstrates that the performance of the PSC is directly impacted by altering the N_A of the HTL, while Figure 13c,d shows the behaviors of J_{sc} and FF. The N_A of the HTL is increased from 1×10^{15} to 1×10^{20} cm^{-3}. The findings demonstrate that the V_{oc} and PCE of the structures significantly improved as the N_A rose. Structures with CMTS and CZTS were greatly improved by increasing the doping content of the HTL, whereas the remaining structures either remained constant or showed a minor improvement in terms of their V_{oc} and PCE.

3.8. Metal Oxide ETL Doping Optimization. The final phase in the device optimization of the PSC is the optimization of the doping concentration (N_D) of ETL. Doping ETL enhances the PSC's conductivity, stability, and affinity for electrons, which ultimately enhances the cell's performance.[19,42,43]

Figure 14a,b shows that the N_D for ETL in this work is varied from 1×10^{15} to 1×10^{20} cm^{-3} to analyze its effect on the V_{oc} and PCE of the PSCs. Figure 14a shows the N_D effect on V_{oc} of PSCs, and it can be seen that the V_{oc} of the cells either stayed constant or increased a little. Overall, there is no degradation in the V_{oc} of all of the structures. Figure 14b shows that increasing the N_D in the $CsSnGeI_3$ layer also followed the same trend, where the structures either remained constant or showed an increase in PCE. Figure 14c,d shows the behaviors of J_{sc} and FF. Overall, there is no degradation in the PCE of cells with increased N_D. The device optimization procedure is finished with the optimization of ETLs, and the optimized N_D values for ETLs in the optimized PSCs are given in Table 7.

3.9. Optimized PSCs. The device optimization is carried out for each individual structure by optimizing the thickness and doping content of the $CsSnGeI_3$ perovskite absorber layer and the CTLs. The optimization process is carried out in six steps. The device optimization of the PSCs helped achieve the maximum possible PCE for each structure. The optimum parameters of thickness and doping concentration of each layer are presented in Table 7 along with their $I-V$ characteristics. Figure 15 shows the overlay results for the optimized and nonoptimized $CsSnGeI_3$-based 18 novel PSCs with oxide and kesterite CTLs. The optimization of each individual structure resulted in a significant increase in the PCE of the cell. For the structure of $SnO_2-CsSnGeI_3-CBTS$, the increase in PCE was a whopping 10%. The findings showed that $SnO_2/CsSnGeI_3/CNTS$ is the most efficient PSC among all of the simulated structures, with a PCE of 27.33%, J_{sc} of 28.04 mA/cm^2, FF of 85%, and V_{oc} of 1.14 V.

3.10. Influence of $CsSnGeI_3$ "N_t" on PSCs. The optoelectronic characteristics and PCE of the cell are affected by the flaws in the absorber layer of the PSCs. These defects in the absorber are formed due to vacancies, impurities, and interstitials that act as traps for charge carriers and lead to nonradiative recombination. The generated charge carriers do not contribute to the current when they get caught in traps and are thus lost as heat. To improve the efficiency and stability of the PSC, the defects in the absorber layer should be as less as possible.[12,14,21,44]

Figure 16a–d shows the impact of altering the N_t for the PSCs, and it is varied from 1×10^{12} to 1×10^{18} cm^{-3}. The findings reveal that as the number of defects in the $CsSnGeI_3$ absorber is increased, the J_{sc} and PCE of the cells degrade in all three groups. This is due to the fact that at greater N_t, the absorber material's increased number of traps led to the recombination of electrons and holes, and the current was lost as heat without contributing to the cell's total ability to generate electricity.

3.11. Influence of Interface Defects. The PSC architecture consists of several layers stacked upon one another working together to convert photons into electrical current. The perovskite material is inserted between the CTLs. The different materials produce defects at the absorber/HTL and ETL/absorber interfaces. These defects at the interfaces act as trap states for the charge carriers and lead to recombination, resulting in the loss of current in the form of heat, resultantly lowering the cell's PCE.[33,45,46]

Figure 17a,b shows the influence of altering the interface defects at the ETL/$CsSnGeI_3$ interface, while Figure 17c,d shows the effect of HTL/$CsSnGeI_3$ on the V_{oc} and J_{sc} of the PSCs. The results show that at a lower interface defect value, the performance of the PSCs was not affected, but as the value is raised, the cell performance was substantially degraded. The effects of ETL/$CsSnGeI_3$ and $CsSnGeI_3$/HTL defects on the V_{oc} of all three groups resulted in a downward trend, whereas the PCE of all of the PSCs in the three groups also followed the same behavior.

3.12. Temperature Effect on PSCs. PSCs are temperature-sensitive devices, and a slight change in the temperature may influence the device performance. At lower temperatures, the PSC becomes rigid and less conductive, while at higher temperatures, the CTLs get affected, resulting in inadequate separation and enhanced recombination, thus degrading and decomposing the PSC material quality and efficiency. Ideally, room temperature (293 K) is the best suitable environment for a PSC to work efficiently.[4,24,47]

Figure 18a,b shows that the temperature of the PSCs is varied from 280 to 440 K to investigate the effect on the V_{oc} and PCE of the cells. The findings in Figure 18a revealed that all of the structures had their maximum V_{oc} at 280 K, and as the temperature increased, their V_{oc} started to decrease in all three groups. Moreover, Figure 18b reveals that the PCE of all three groups also followed the same trend with their maximum PCE at room temperature, and then it started to degrade as the temperature increased beyond 280 K. All of the structures had their minimum V_{oc} and PCE at 360 K. Hence, it can be deduced that high temperatures negatively affect the outperformance of the PSCs.

https://doi.org/10.1021/acsomega.3c07754
ACS Omega 2024, 9, 11398−11417

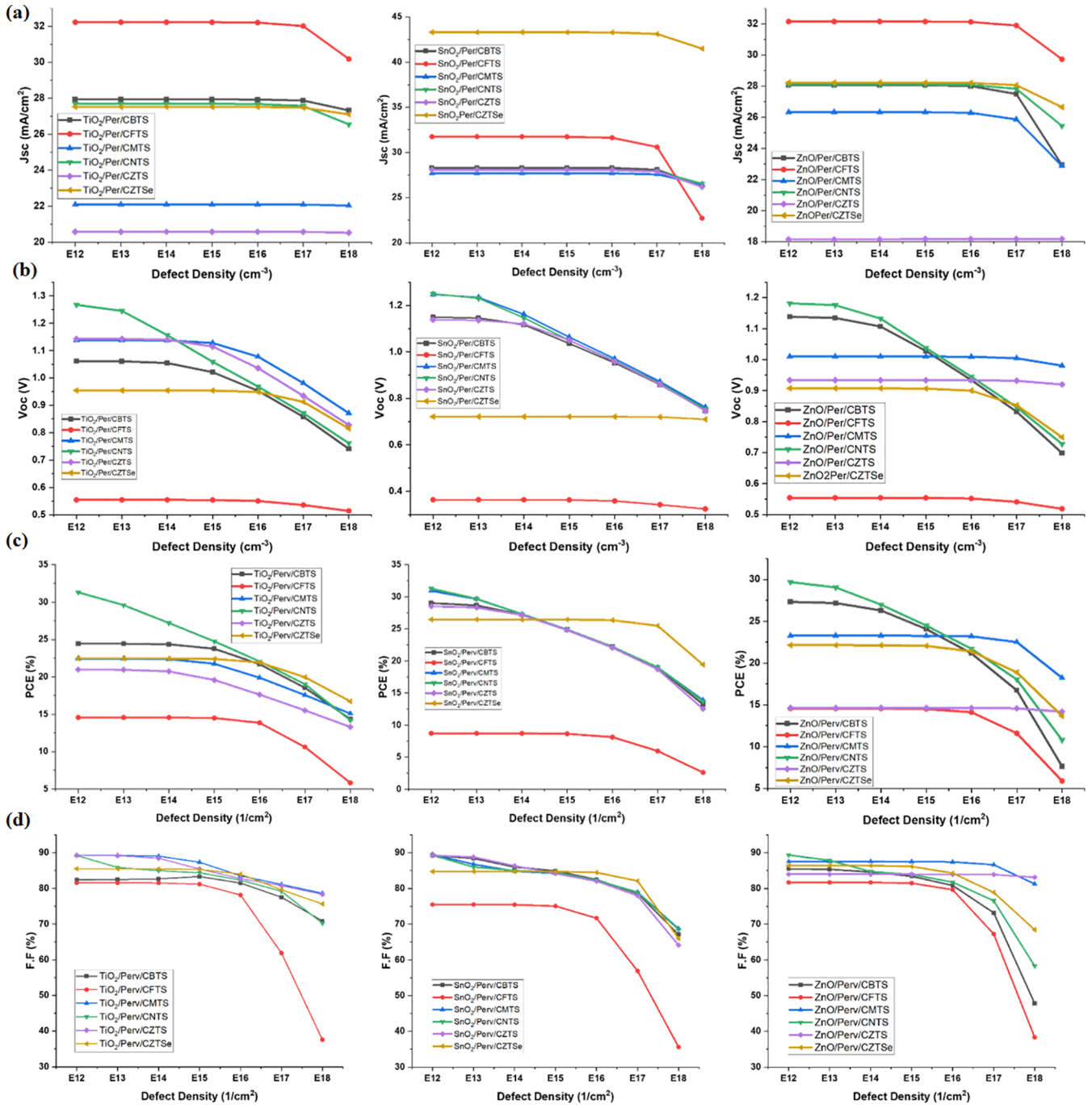

Figure 16. Impact of $CsSnGeI_3$ "N_t" on (a) J_{sc}, (b) V_{oc}, (c) PCE, and (d) FF of PSCs

3.13. Impact of Work Function. The work function (⌀) impacts the $I-V$ characteristics of the PSC. In the PSC, ⌀ is a crucial factor in determining the energy band alignment and the extraction and transportation of charge carriers from the absorber to the CTLs and then to their respective electrodes. Due care should be taken to ensure proper band alignment between the various layers of the PSC. A higher value of the cathode's ⌀, coupled with a lower value of the anode's ⌀, results in a decrease in the overall PCE of the PSCs. Therefore, achieving an optimal balance between the electrodes' ⌀ is crucial for maximizing electron collection and the overall device performance in PSCs. The charge carriers are lost due to the mismatched value of the electrodes ⌀.[21,48]

Figure 19a shows that the ⌀ value of the anode is varied from 4.7 to 6 eV for all of the structures, while Figure 19b shows the ⌀ variation for the cathode from 3.8 to 4.8 eV. The results show that varying the anode's ⌀ affected the PCE of PSCs in all groups. As the anode's ⌀ is increased from 4.7 to 5.1 eV, a rise in PCE can be observed for all of the structures, especially for structures with CMTS, CNTS, and CZTS HTLs. Beyond 5.1 eV, the cells show saturation as the PCEs remain constant or have a negligible effect. Figure 19b shows that as the value of the cathode's ⌀ is increased beyond 4.4 eV for all of the structures, the PCE of all of the structures in the three groups showed a downward trend with a higher ⌀ value of the cathode material. The ETL has optimal performance on a low work function.

https://doi.org/10.1021/acsomega.3c07754
ACS Omega 2024, 9, 11398−11417

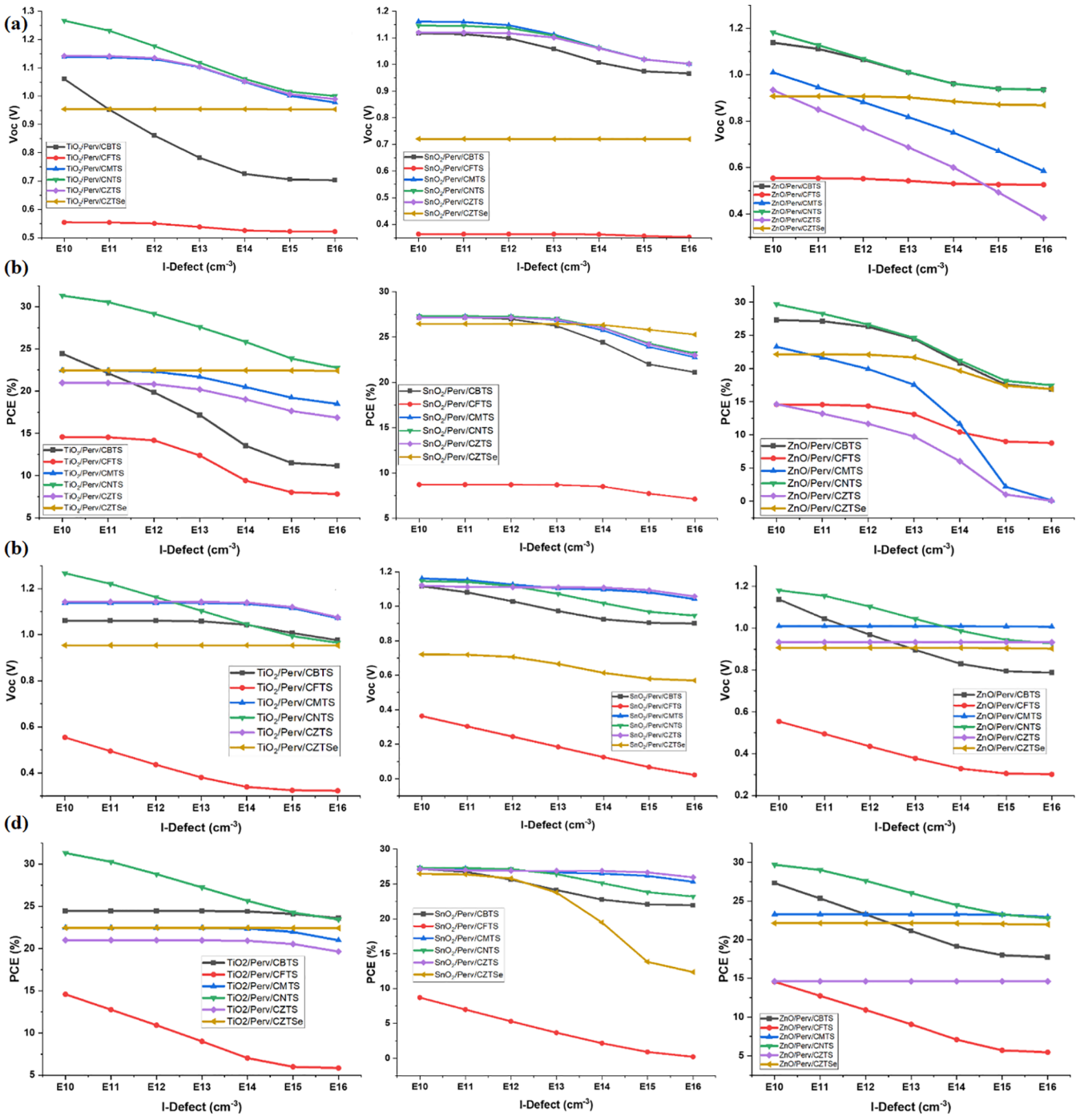

Figure 17. CTL/$CsSnGeI_3$ interface defect effect on (a) J_{sc}, (b) V_{oc}, (c) PCE, and (d) FF of PSCs.

4. CONCLUSIONS

In this work, 18 PSCs were numerically modeled and optimized by using various combinations of CTLs with the nontoxic $CsSnGeI_3$ perovskite absorber layer using SCAPS-1D. All of the simulations were carried out under STC. The three ETL materials chosen are metal oxide TiO_2, SnO_2, and ZnO, while the six kesterite quaternary materials chosen are HTLs. The absorption of the light spectrum and the effect of CTLs on the QE of the PSCs were investigated along with their energy band alignment, built-in electric field, and rate of recombination at various interfaces. To enhance the PCE of the PSCs, optimization of thickness and doping concentration of each layer in the device architecture were carried out to achieve the maximum possible PCE for each individual structure. The device optimization of the PSCs helped enhance the PCE for some structures by more than 4%. Additionally, the effect of defects at the ETL/$CsSnGeI_3$ and $CsSnGeI_3$/HTL interfaces as well as the impact of defect density in the $CsSnGeI_3$ perovskite absorber on the overall performance of the PSCs was carefully examined. In the modeled PSCs, the influence of working temperature and the function of work are shown in detail.

The simulation findings revealed that the most efficient nonoptimized PSC among all 18 structures is SnO_2−$CsSnGeI_3$−CMTS with a J_{sc} of 25.22 mA/cm^2, V_{oc} of 1.12 V, FF of 87%, and PCE of 24.64%, while the least efficient

https://doi.org/10.1021/acsomega.3c07754
ACS Omega 2024, 9, 11398−11417

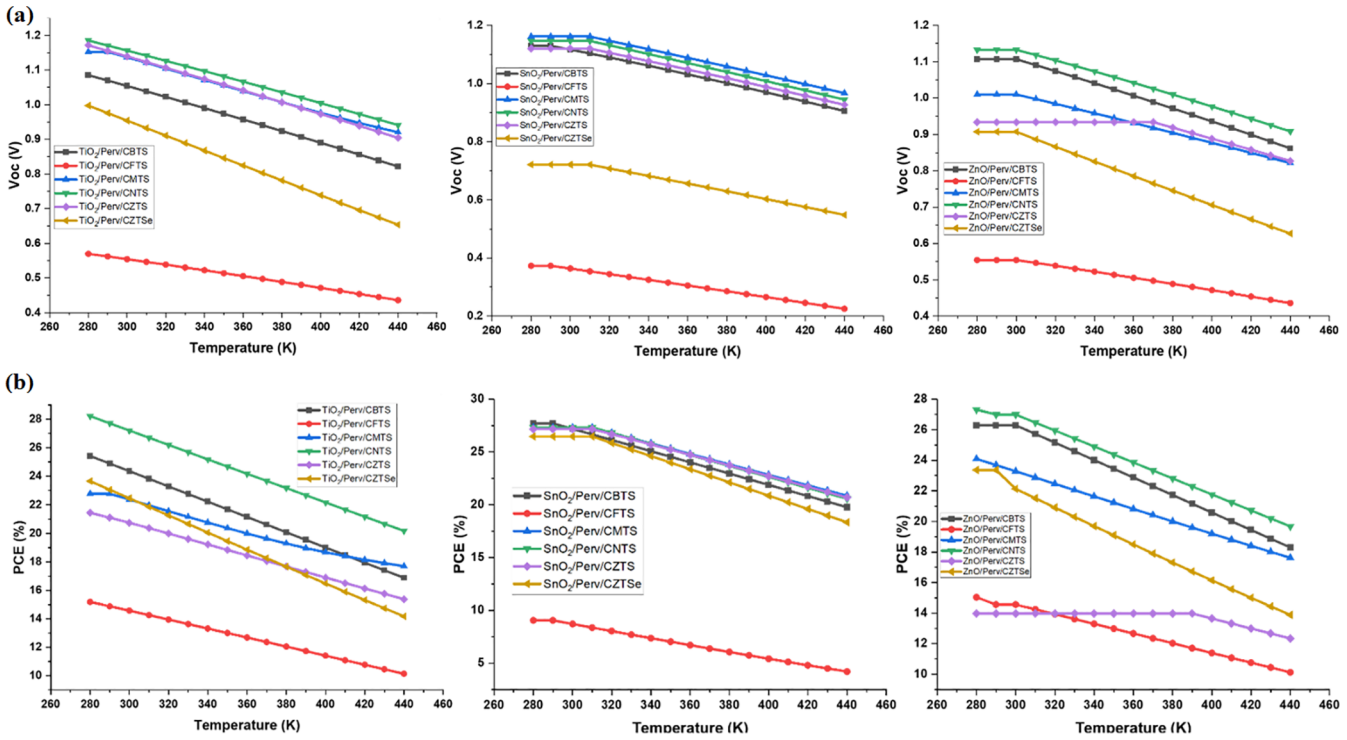

Figure 18. Impact of temperature on (a) V_{oc} and (b) PCE.

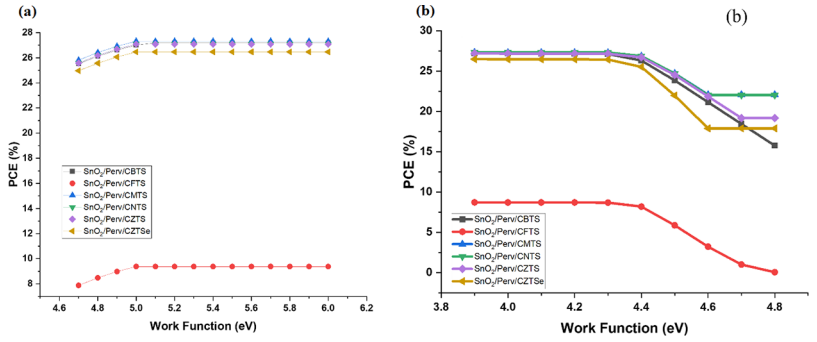

Figure 19. Effect on PCE due to (a) anode's ⌀ and (b) cathode's ⌀.

nonoptimized PSC structure is ZnO-$CsSnGeI_3$−CZTS with a J_{sc} of 15.69 mA/cm^2, V_{oc} of 0.96 V, FF of 38.77%, and PCE of 5.88%. The optimization of each individual structure resulted in a massive increase in the PCE of the cell; for a structure SnO_2−$CsSnGeI_3$−CBTS, the increase in PCE was a whopping 10%. The simulation findings also demonstrated that SnO_2−$CsSnGeI_3$−CNTS is the most efficient optimized-PSC among all of the optimized simulated structures, with a PCE of 27.33%, J_{sc} of 28.04 mA/cm^2, FF of 85%, and V_{oc} of 1.14 V, whereas the structure with CFTS as HTL had overall performed worse in all three ETL-based groups. This study provides a detailed guideline for the fabrication of Pb-free mixed tin−germanium PSCs.

AUTHOR INFORMATION

Corresponding Authors

Muhammad Noman − *U.S.-Pakistan Center for Advanced Studies in Energy, University of Engineering and Technology, Peshawar 25000, Pakistan;* orcid.org/0000-0001-8718-6386; Email: muhammad.noman@uetpeshawar.edu.pk

Affaq Qamar − *Imam Mohammad Ibn Saud Islamic University (IMSIU), Riyadh 11564, Kingdom of Saudi Arabia;* Email: aaqamar@imamu.edu.sa

Authors

Ihsan Nawaz Khan − *U.S.-Pakistan Center for Advanced Studies in Energy, University of Engineering and Technology, Peshawar 25000, Pakistan*

Khalid AlSnaie − *Imam Mohammad Ibn Saud Islamic University (IMSIU), Riyadh 11564, Kingdom of Saudi Arabia*

Hassan M. Hussein Farh − *Imam Mohammad Ibn Saud Islamic University (IMSIU), Riyadh 11564, Kingdom of Saudi Arabia*

Complete contact information is available at: https://pubs.acs.org/10.1021/acsomega.3c07754

Notes

The authors declare no competing financial interest.

https://doi.org/10.1021/acsomega.3c07754
ACS Omega 2024, 9, 11398−11417

■ ACKNOWLEDGMENTS

This work was supported and funded by the Deanship of Scientific Research at Imam Mohammad Ibn Saud Islamic University (IMSIU) (grant number IMSIU-RG23022).

■ REFERENCES

(1) Katz, E. A. Perovskite: Name Puzzle and German-Russian Odyssey of Discovery. *Helv. Chim. Acta* **2020**, *103* (6), No. e2000061.
(2) Kumar, N. S.; Naidu, K. C. B. A Review on Perovskite Solar Cells (PSCs), Materials and Applications. *J. Mater.* **2021**, *7* (5), 940−956, DOI: 10.1016/j.jmat.2021.04.002.
(3) https://www.nrel.gov/pv/interactive-cell-efficiency.html.
(4) Roy, P.; Tiwari, S.; Khare, A. An Investigation on the Influence of Temperature Variation on the Performance of Tin (Sn) Based Perovskite Solar Cells Using Various Transport Layers and Absorber Layers. *Results Opt.* **2021**, *4*, No. 100083.
(5) Kour, R.; Arya, S.; Verma, S.; Gupta, J.; Bandhoria, P.; Bharti, V.; Datt, R.; Gupta, V. Potential Substitutes for Replacement of Lead in Perovskite Solar Cells: A Review. *Glob. Challenges* **2019**, *3* (11), No. 1900050.
(6) Nayak, M.; Akthar, A. J.; Guchhait, A.; Saha, S. K. A Roadmap towards Stable Perovskite Solar Cells: Prospective on Substitution of Organic (A) & Inorganic (B) Cations. *J. Mater. Sci.: Mater. Electron.* **2021**, *32* (14), 18466−18511.
(7) Khan, Z.; Noman, M.; Jan, S. T.; Khan, A. D. Systematic Investigation of the Impact of Kesterite and Zinc Based Charge Transport Layers on the Device Performance and Optoelectronic Properties of Ecofriendly Tin (Sn) Based Perovskite Solar Cells. *Sol. Energy* **2023**, *257*, 58−87, DOI: 10.1016/j.solener.2023.04.019.
(8) Bhattarai, S.; Pandey, R.; Madan, J.; Ahmed, F.; Shabnam, S. Performance Improvement Approach of All Inorganic Perovskite Solar Cell with Numerical Simulation. *Mater. Today Commun.* **2022**, *33*, No. 104364.
(9) Pitaro, M.; Tekelenburg, E. K.; Shao, S.; Loi, M. A. Tin Halide Perovskites: From Fundamental Properties to Solar Cells. *Adv. Mater.* **2022**, *34* (1), No. 2105844, DOI: 10.1002/adma.202105844.
(10) Aftab, A.; Ahmad, M. I. A Review of Stability and Progress in Tin Halide Perovskite Solar Cell. *Sol. Energy* **2021**, *216*, 26−47.
(11) Chen, M.; Ju, M. G.; Garces, H. F.; Carl, A. D.; Ono, L. K.; Hawash, Z.; Zhang, Y.; Shen, T.; Qi, Y.; Grimm, R. L.; Pacifici, D.; Zeng, X. C.; Zhou, Y.; Padture, N. P. Highly Stable and Efficient All-Inorganic Lead-Free Perovskite Solar Cells with Native-Oxide Passivation. *Nat. Commun.* **2019**, *10* (1), No. 16, DOI: 10.1038/s41467-018-07951-y.
(12) Jan, S. T.; Noman, M. Influence of Layer Thickness, Defect Density, Doping Concentration, Interface Defects, Work Function, Working Temperature and Reflecting Coating on Lead-Free Perovskite Solar Cell. *Sol. Energy* **2022**, *237*, 29−43, DOI: 10.1016/j.solener.2022.03.069.
(13) Jan, S. T.; Noman, M. Influence of Absorption, Energy Band Alignment, Electric Field, Recombination, Layer Thickness, Doping Concentration, Temperature, Reflection and Defect Densities on MAGeI 3 Perovskite Solar Cells with Kesterite HTLs. *Phys. Scr.* **2022**, *97* (12), No. 125007, DOI: 10.1088/1402-4896/ac9e7f.
(14) Nalianya, M. A.; Awino, C.; Barasa, H.; Odari, V.; Gaitho, F.; Omogo, B.; Mageto, M. Numerical Study of Lead Free CsSn0.5Ge0.5I3 Perovskite Solar Cell by SCAPS-1D. *Optik* **2021**, *248*, No. 168060.
(15) Singh, N.; Agarwal, A.; Agarwal, M. Numerical Simulation of Highly Efficient Lead-Free Perovskite Layers for the Application of All-Perovskite Multi-Junction Solar Cell. *Superlattices Microstruct.* **2021**, *149*, No. 106750, DOI: 10.1016/j.spmi.2020.106750.
(16) Tonui, P.; Oseni, S. O.; Sharma, G.; Yan, Q.; Mola, G. T. Perovskites Photovoltaic Solar Cells: An Overview of Current Status. *Renewable Sustainable Energy Rev.* **2018**, *91*, 1025−1044, DOI: 10.1016/j.rser.2018.04.069.
(17) Le Corre, V. M.; Stolterfoht, M.; Perdigón Toro, L.; Feuerstein, M.; Wolff, C.; Gil-Escrig, L.; Bolink, H. J.; Neher, D.; Koster, L. J. A. Charge Transport Layers Limiting the Efficiency of Perovskite Solar Cells: How to Optimize Conductivity, Doping, and Thickness. *ACS Appl. Energy Mater.* **2019**, *2* (9), 6280−6287.
(18) Ravishankar, S.; Gharibzadeh, S.; Roldán-Carmona, C.; Grancini, G.; Lee, Y.; Ralaiarisoa, M.; Asiri, A. M.; Koch, N.; Bisquert, J.; Nazeeruddin, M. K. Influence of Charge Transport Layers on Open-Circuit Voltage and Hysteresis in Perovskite Solar Cells. *Joule* **2018**, *2* (4), 788−798.
(19) Bag, A.; Radhakrishnan, R.; Nekovei, R.; Jeyakumar, R. Effect of Absorber Layer, Hole Transport Layer Thicknesses, and Its Doping Density on the Performance of Perovskite Solar Cells by Device Simulation. *Sol. Energy* **2020**, *196*, 177−182.
(20) Hossain, M. K.; Rubel, M. H. K.; Toki, G. F. I.; Alam, I.; Rahman, M. F.; Bencherif, H. Effect of Various Electron and Hole Transport Layers on the Performance of CsPbI 3 -Based Perovskite Solar Cells: A Numerical Investigation in DFT, SCAPS-1D, and WxAMPS Frameworks. *ACS Omega* **2022**, *7*, 43210−43230, DOI: 10.1021/acsomega.2c05912.
(21) Islam, M. S.; Sobayel, K.; Al-Kahtani, A.; Islam, M. A.; Muhammad, G.; Amin, N.; Shahiduzzaman, M.; Akhtaruzzaman, M. Defect Study and Modelling of SnX3-Based Perovskite Solar Cells with SCAPS-1D. *Nanomaterials* **2021**, *11* (5), No. 1218, DOI: 10.3390/nano11051218.
(22) Jan, S. T.; Noman, M. Comprehensive Analysis of Heterojunction Compatibility of Various Perovskite Solar Cells with Promising Charge Transport Materials. *Sci. Rep.* **2023**, *13* (1), No. 19015, DOI: 10.1038/s41598-023-46482-5.
(23) Jan, S. T.; Noman, M. Analyzing the Effect of Planar and Inverted Structure Architecture on the Properties of MAGeI3 Perovskite Solar Cells. *Energy Technol.* **2023**, *11* (11), No. 2300564, DOI: 10.1002/ente.202300564.
(24) Karimi, E.; Ghorashi, S. M. B. The Effect of SnO2 and ZnO on the Performance of Perovskite Solar Cells. *J. Electron. Mater.* **2020**, *49* (1), 364−376.
(25) Gulomov, J.; Accouche, O.; Aliev, R.; Neji, B.; Ghandour, R.; Gulomova, I.; Azab, M. Geometric Optimization of Perovskite Solar Cells with Metal Oxide Charge Transport Layers. *Nanomaterials* **2022**, *12* (15), No. 2692, DOI: 10.3390/nano12152692.
(26) Hossain, M. K.; Toki, G. F. I.; Alam, I.; Pandey, R.; Samajdar, D. P.; Rahman, M. F.; Islam, M. R.; Rubel, M. H. K.; Bencherif, H.; Madan, J.; Mohammed, M. K. A. Numerical Simulation and Optimization of a CsPbI3-Based Perovskite Solar Cell to Enhance the Power Conversion Efficiency. *New J. Chem.* **2023**, *47* (10), 4801−4817.
(27) Khattak, Y. H.; Baig, F.; Toura, H.; Beg, S.; Soucase, B. M. CZTSe Kesterite as an Alternative Hole Transport Layer for MASnI3 Perovskite Solar Cells. *J. Electron. Mater.* **2019**, *48* (9), 5723−5733.
(28) Khattak, Y. H.; Baig, F.; Shuja, A.; Beg, S.; Soucase, B. M. Numerical Analysis Guidelines for the Design of Efficient Novel Nip Structures for Perovskite Solar Cell. *Sol. Energy* **2020**, *207*, 579−591.
(29) Roy, P.; Ghosh, A.; Barclay, F.; Khare, A.; Cuce, E. Perovskite Solar Cells: A Review of the Recent Advances. *Coatings* **2022**, *12* (8), No. 1089, DOI: 10.3390/coatings12081089.
(30) Salim, T.; Sun, S.; Abe, Y.; Krishna, A.; Grimsdale, A. C.; Lam, Y. M. Perovskite-Based Solar Cells: Impact of Morphology and Device Architecture on Device Performance. *J. Mater. Chem. A* **2015**, *3* (17), 8943−8969.
(31) Sutton, R. J.; Eperon, G. E.; Miranda, L.; Parrott, E. S.; Kamino, B. A.; Patel, J. B.; Hörantner, M. T.; Johnston, M. B.; Haghighirad, A. A.; Moore, D. T.; Snaith, H. J. Bandgap-Tunable Cesium Lead Halide Perovskites with High Thermal Stability for Efficient Solar Cells. *Adv. Energy Mater.* **2016**, *6* (8), No. 150248, DOI: 10.1002/aenm.201502458.
(32) Nishimura, K.; Kamarudin, M. A.; Hirotani, D.; Hamada, K.; Shen, Q.; Iikubo, S.; Minemoto, T.; Yoshino, K.; Hayase, S. Lead-Free Tin-Halide Perovskite Solar Cells with 13% Efficiency. *Nano Energy* **2020**, *74*, No. 104858.
(33) Sherkar, T. S.; Momblona, C.; Gil-Escrig, L.; Ávila, J.; Sessolo, M.; Bolink, H. J.; Koster, L. J. A. Recombination in Perovskite Solar Cells: Significance of Grain Boundaries, Interface Traps, and Defect Ions. *ACS Energy Lett.* **2017**, *2* (5), 1214−1222.

https://doi.org/10.1021/acsomega.3c07754
ACS Omega 2024, 9, 11398−11417

(34) Głowienka, D.; Zhang, D.; Di Giacomo, F.; Najafi, M.; Veenstra, S.; Szmytkowski, J.; Galagan, Y. Role of Surface Recombination in Perovskite Solar Cells at the Interface of HTL/CH3NH3PbI3. *Nano Energy* **2020**, *67*, No. 104186, DOI: 10.1016/j.nanoen.2019.104186.
(35) Chen, J.; Park, N. G. Causes and Solutions of Recombination in Perovskite Solar Cells. *Adv. Mater.* **2019**, *31* (47), No. 1803019.
(36) Maram, D. K.; Haghighi, M.; Shekoofa, O.; Habibiyan, H.; Ghafoorifard, H. A Modeling Study on Utilizing Ultra-Thin Inorganic HTLs in Inverted p−n Homojunction Perovskite Solar Cells. *Sol. Energy* **2021**, *213*, 1−12, DOI: 10.1016/j.solener.2020.11.009.
(37) Yu, X.; Zou, X.; Cheng, J.; Chang, C.; Zhou, Z.; Li, G.; Liu, B.; Wang, J.; Chen, D.; Yao, Y. Numerical Simulation Analysis of Effect of Energy Band Alignment and Functional Layer Thickness on the Performance for Perovskite Solar Cells with Cd1-XZnxS Electron Transport Layer. *Mater. Res. Express* **2020**, *7* (10), No. 105906, DOI: 10.1088/2053-1591/abbf12.
(38) De Los Santos, I. M.; Cortina-Marrero, H. J.; Ruíz-Sánchez, M. A.; Hechavarría-Difur, L.; Sánchez-Rodríguez, F. J.; Courel, M.; Hu, H. Optimization of CH3NH3PbI3 Perovskite Solar Cells: A Theoretical and Experimental Study. *Sol. Energy* **2020**, *199*, 198−205, DOI: 10.1016/j.solener.2020.02.026.
(39) Tara, A.; Bharti, V.; Sharma, S.; Gupta, R. Device Simulation of FASnI3 Based Perovskite Solar Cell with Zn(O0.3, S0.7) as Electron Transport Layer Using SCAPS-1D. *Opt. Mater.* **2021**, *119*, No. 111362.
(40) Abdelaziz, S.; Zekry, A.; Shaker, A.; Abouelatta, M. Investigating the Performance of Formamidinium Tin-Based Perovskite Solar Cell by SCAPS Device Simulation. *Opt. Mater.* **2020**, *101*, No. 109738.
(41) Raghvendra; Kumar, R. R.; Pandey, S. K. Performance Evaluation and Material Parameter Perspective of Eco-Friendly Highly Efficient CsSnGeI3 Perovskite Solar Cell. *Superlattices Microstruct.* **2019**, *135*, No. 106273, DOI: 10.1016/j.spmi.2019.106273.
(42) Agha, D. N. Q.; Algwari, Q. T. The Influence of the Conduction Band Engineering on the Perovskite Solar Cell Performance. *Results Opt.* **2022**, *9*, No. 100291.
(43) Roy, P.; Khare, A. Analysis of an Efficient and Eco-Friendly CsGeSnI3based Perovskite Solar Cell: A Theoretical Study. *Mater. Today Proc.* **2021**, *44*, 2997−3000.
(44) Kanoun, A. A.; Kanoun, M. B.; Merad, A. E.; Goumri-Said, S. Toward Development of High-Performance Perovskite Solar Cells Based on CH3NH3GeI3 Using Computational Approach. *Sol. Energy* **2019**, *182*, 237−244.
(45) Izadi, F.; Ghobadi, A.; Gharaati, A.; Minbashi, M.; Hajjiah, A. Effect of Interface Defects on High Efficient Perovskite Solar Cells. *Optik* **2021**, *227*, No. 166061.
(46) Azri, F.; Meftah, A.; Sengouga, N.; Meftah, A. Electron and Hole Transport Layers Optimization by Numerical Simulation of a Perovskite Solar Cell. *Sol. Energy* **2019**, *181*, 372−378.
(47) Roy, P.; Sinha, N. K.; Khare, A. An Investigation on the Impact of Temperature Variation over the Performance of Tin-Based Perovskite Solar Cell: A Numerical Simulation Approach. *Mater. Today Proc.* **2021**, *39*, 2022−2026.
(48) Simya, O. K.; Mahaboobbatcha, A.; Balachander, K. A Comparative Study on the Performance of Kesterite Based Thin Film Solar Cells Using SCAPS Simulation Program. *Superlattices Microstruct.* **2015**, *82*, 248−261.

https://doi.org/10.1021/acsomega.3c07754
ACS Omega 2024, 9, 11398−11417